

Multi-target Range, Doppler and Angle estimation in MIMO-FMCW Radar with Limited Measurements

Chandrashekhar Rai*, Himali Singh* and Arpan Chattopadhyay

Abstract—Multiple-input multiple-output (MIMO) radar offers several performance and flexibility advantages over traditional radar arrays. However, high angular and Doppler resolutions necessitate a large number of antenna elements and the transmission of numerous chirps, leading to increased hardware and computational complexity. While compressive sensing (CS) has recently been applied to pulsed-waveform radars with sparse measurements, its application to frequency-modulated continuous wave (FMCW) radar for target detection remains largely unexplored. In this paper, we propose a novel CS-based multi-target localization algorithm in the range, Doppler, and angular domains for MIMO-FMCW radar, where we jointly estimate targets' velocities and angles of arrival. To this end, we present a signal model for sparse-random and uniform linear arrays based on three-dimensional spectral estimation. For range estimation, we propose a discrete Fourier transform (DFT)-based focusing and orthogonal matching pursuit (OMP)-based techniques, each with distinct advantages, while two-dimensional CS is used for joint Doppler-angle estimation. Leveraging the properties of structured random matrices, we establish theoretical uniform and non-uniform recovery guarantees with high probability for the proposed framework. Our numerical experiments demonstrate that our methods achieve similar detection performance and higher resolution compared to conventional DFT and MUSIC with fewer transmitted chirps and antenna elements.

Index Terms—FMCW radar, MIMO radar, range-Doppler-angle estimation, sparse linear arrays, 2D-compressive sensing.

I. INTRODUCTION

Sensing the environment using radar or other sensors is an integral part of many engineering applications. A radar usually localizes a target of interest by estimating its range, Doppler velocity, and angle of arrival (AoAs). Owing to their portability, low cost, and high range resolution, frequency-modulated continuous wave (FMCW) radars are often preferred in short-range applications like advanced driving assistance systems (ADAS) [2, 3], synthetic aperture radars (SARs) [4, 5], surveillance systems [6, 7], and human vital sign monitoring [8]. FMCW radars transmit a finite number of linear frequency-modulated (LFM) chirps in each coherent processing interval (CPI). The receiver mixes the signal reflected from targets with the transmitted signal, producing a complex sinusoidal intermediate frequency (IF) signal. The IF signal's frequencies then determine the target ranges and velocities. To further localize targets in the angular domain, an array of multiple transmitter and receiver antennas is required. Multiple-input multiple-output (MIMO) radars transmit multiple orthogonal waveforms and jointly process the target returns across multiple receivers, providing additional degrees of freedom and higher resolution compared to conventional phased array radars, but with fewer physical antenna elements.

Traditionally, the discrete Fourier transform (DFT) has been used to estimate the frequencies present in the IF signal [2, 9]. However, in this approach, the range and velocity resolutions depend on the bandwidth and CPI. Achieving high range resolution necessitates large bandwidths, while high velocity resolution requires transmitting and processing a large number of chirps. Similarly, array processing theory dictates that achieving a high angular resolution demands

a large array aperture with numerous antenna elements to avoid ambiguities [10]. Although MIMO technology enhances angular resolution, synthesizing a large virtual array with half-wavelength element spacing can be costly. Consequently, increasing resolution results in greater hardware and computational complexity. In order to mitigate these challenges, subspace-based parameter estimation techniques have been proposed in the literature. Multiple signal classification (MUSIC) has been introduced for range and angle estimation in [11, 12]. Estimation of signal parameters via rotational techniques (ESPRIT) is suggested in [13], while [14] explores a joint DFT-ESPRIT framework. Array interpolation and eigenstructure methods are investigated in [15].

Although subspace-based methods offer high resolutions, they have several drawbacks. These methods typically assume non-coherent sources or require additional smoothing in the coherent case. Additionally, they often necessitate prior knowledge of the number of targets to be estimated. The computational complexity of these methods escalate significantly when estimating parameters in multi-dimensional signals. Recently, compressive sensing (CS) has emerged as an efficient technique for sparse signal recovery with limited measurements [16]. By utilizing a user-defined parameter grid, CS facilitates high-resolution estimation with a small number of measurements and low computational efforts. In this work, we utilize CS techniques in MIMO-FMCW radars for range and joint velocity-angle estimation at high resolutions but using a small number of antenna elements and transmitted chirps. Note that in radar, the sampled IF signal, chirps in each CPI, and array channels correspond to measurements across different domains, known as fast-time, slow-time, and spatial domain samples, respectively. Additionally, we investigate the theoretical recovery guarantees for our joint velocity-angle estimation framework and demonstrate the performance of our proposed method through extensive numerical experiments.

A. Prior Art

Earlier CS applications in radar systems typically focused on uniform sampling or full measurements. In [17], CS replaced the matched filter reducing the sampling rate for radar imaging, while [18, 19] explored high-resolution estimation in a general 2D time-frequency domain. Efficient waveforms to reconstruct sparse targets were suggested in [20]. In [21, 22], the randomized measurement framework was utilized for radar imaging in remote sensing and inverse SAR applications. A CS-based constant false alarm rate (CFAR) detector was developed in [23] while [24] used CS to leverage the diversity of various array orientations for high-resolution spatial spectrum reconstruction. Recently, [25] proposed a two-level CS-based compression technique for fast target detection in MIMO radar compared to conventional methods.

A key benefit of CS techniques is the reduction in measurement requirements for sparse signals. In radar, the target scene is sparse because only a few targets are typically present, making CS a natural fit for the problem. As a result, CS has been widely adopted to enable sub-Nyquist radars with reduced measurements [26–28]. In the spatial domain, sparse linear arrays (SLAs), with fewer antenna elements compared to uniform linear arrays (ULAs), have been introduced for both pulsed and continuous-wave radars [9, 29, 30]. Optimal sparse

*Co-first authors.

All authors are with the Electrical Engineering Department, Indian Institute of Technology (IIT) Delhi, India. Email: csrai.cstaff@iitd.ac.in, ez208426@ee.iitd.ac.in, arpanc@ee.iitd.ac.in.

The conference precursor of this work is [1].

array design was investigated in [30], while [9] designed a non-uniform SLA and applied digital beamforming for AOA estimation after interpolating the missing measurements. Conversely, [29] suggested matrix completion methods to reconstruct the corresponding linear array. Although these methods involve sparse measurements, they complete the missing measurements before parameter estimation, resulting in a high computational load at the receiver.

Alternatively, spatial CS enables direct parameter recovery from SLAs [31, 32]. For instance, [31] focused on pulsed-MIMO radar and estimated AOAs for a specific range-velocity bin using different CS recovery algorithms. Additionally, [33] incorporated velocity estimation but not range. In [32], velocities and angles were estimated using measurements from a small number of randomly positioned transmitters and receivers on a circular disc. Besides spatial compression, CS techniques have also been applied in radar systems for interference mitigation [34], spectrum sharing [35], joint radar-communication systems [36], and multi-target shadowing effect mitigation [37]. Furthermore, [38] discussed the advantages and challenges of applying CS in radar, including clutter cancellation. However, these earlier works primarily concentrated on pulsed-wave radars, leaving CS-based joint parameter estimation in FMCW radars largely unexplored.

B. Our contributions

Preliminary results of this work appeared in our conference publication [1], where we addressed range and angle estimation only, without any theoretical guarantees. In this work, we consider a MIMO-FMCW radar with a random SLA that transmits only a subset of chirps per CPI and present a joint Doppler-angle estimation framework. The reduced number of antenna elements and chirps correspond to spatial and slow-time CS, respectively. Our main contributions in this paper are:

- 1) Range estimation:** Prior works on CS-based radars have mainly focused on pulsed-wave radars and/or recovering target angles and velocities within a specific range bin. In this paper, we first present a separable mixture model for the IF signal, applicable to both full and sparse measurements. We propose two methods for range estimation: (a) DFT-focusing followed by binary integration [10], and (b) range-orthogonal matching pursuit (range-OMP). Binary integration improves detection at low SNRs, while OMP provides higher resolution and reduced computational costs; see Remarks 2-3.
- 2) Joint Doppler-angle estimation:** We jointly estimate target velocities and AOAs within each detected range bin using both vectorized and joint 2D CS techniques. Our methods deliver performance comparable to that of a full measurement system, with user-defined grids allowing for higher velocity and angular resolutions. Additionally, processing fewer measurements reduces computational complexity and enables the radar to explore multiple angular sectors simultaneously in a single CPI.
- 3) Recovery guarantees:** CS provides approximate solutions for the sparse recovery problem, with sufficient conditions for high-probability recovery being widely studied. In our work, we examine both uniform and non-uniform guarantees and establish bounds on the number of measurements and recovery errors. Specifically, we show that our random but structured measurement matrix exhibits low coherence and satisfies the isotropy property, provided the transmitted chirps, random antenna elements, and velocity-angle grids meet suitable conditions. Deriving these theoretical guarantees is challenging due to the increased dimensionality of the recovered parameters and the interdependence of rows and columns in the measurement matrix. We also present a practical MIMO-FMCW radar setup that satisfies these conditions.
- 4) Comprehensive evaluation:** We consider the detection perfor-

mance of our CS-based methods, including receiver operator characteristic (ROC) and time complexity, and compare them to the classical-DFT and subspace-based MUSIC methods, which rely on full measurements. Our approach achieves similar detection probabilities as these full-measurement techniques but with only half the number of transmitted chirps and physical antenna elements. Additionally, range-OMP and CS-based joint Doppler-angle estimation outperform DFT-based methods in terms of accuracy, while offering resolution comparable to MUSIC at a significantly lower computational complexity.

The rest of the paper is organized as follows. The next section introduces the MIMO-FMCW radar's system model generalized for both full and sparse measurements. Section III develops the CS-based parameter estimation methods while Section IV provides the theoretical recovery guarantees. In Section V, we illustrate the performance of the proposed methods through extensive numerical experiments before concluding in Section VI.

Throughout the paper, we reserve boldface lowercase and uppercase letters for vectors (column vectors) and matrices, respectively, and $\{a_i\}_{i_1 \leq i \leq i_2}$ (or simply $a_{i_1 \leq i \leq i_2}$) denotes a set of elements indexed by an integer i . The notations $[\mathbf{A}]_{:,i}$, $[\mathbf{A}]_{i,:}$ and $[\mathbf{A}]_{i,j}$ denote the i -th column, i -th row and (i,j) -th element of matrix \mathbf{A} , respectively. The transpose/ Hermitian/conjugate operation is $(\cdot)^T/H/*$, expectation/probability is $\mathbb{E}/\mathbb{P}[\cdot]$, the outer product is \otimes and the complement of a set is $(\cdot)^c$. The $l_{2/1/0}$ norm of a vector is $\|\cdot\|_{2/1/0}$. The notations *supp*, *diag*, and *vec* denote support, diagonal matrix, and vectorization, respectively. Also, \mathbf{I}_n and $\mathbf{0}$ denote a ' $n \times n$ ' identity matrix and an all-zero matrix, respectively. We represent the circular-normal and real-valued normal distributions as $\mathcal{CN}(\boldsymbol{\mu}, \mathbf{Q})$ and $\mathcal{N}(\boldsymbol{\mu}, \mathbf{Q})$ (with mean $\boldsymbol{\mu}$ and covariance matrix \mathbf{Q}) while $\mathcal{U}[a, b]/\mathcal{U}\{a_i\}_{i_1 \leq i \leq i_2}$ represents a uniform/ discrete-uniform distribution over interval $[a, b]$ / set $\{a_i\}_{i_1 \leq i \leq i_2}$.

II. SYSTEM MODEL

Consider a monostatic MIMO radar system, as shown in Fig. 1a, consisting of N_T transmitters and N_R receivers located over a (possibly overlapping) array of apertures A_T and A_R , respectively. We define $A \doteq A_T + A_R$. The n -th transmitter and m -th receiver are located at $A\alpha_n/2$ and $A\beta_m/2$ (along the array length), respectively, where $\alpha_n \in [-A_T/A, A_T/A]$ and $\beta_m \in [-A_R/A, A_R/A]$. For a random SLA, $\{\alpha_n\}_{1 \leq n \leq N_T}$ and $\{\beta_m\}_{1 \leq m \leq N_R}$ are drawn i.i.d. from distributions \mathcal{P}_α and \mathcal{P}_β , respectively. In a ULA, $\{\alpha_n\}$ and $\{\beta_m\}$ correspond to the uniformly-spaced transmitter and receiver locations, which results in a virtual array of half-wavelength element spacing, i.e., the spatial Nyquist sampling rate. Note that our random SLA differs from the index-modulation-based joint radar-communication setup of [36], wherein $\{\alpha_n\}$ are selected according to the message communicated while $\{\beta_m\}$ correspond to a uniform receiver array.

The transmitters transmit orthogonal LFM chirps of carrier frequency f_c , chirp rate γ , and chirp duration T_c . The wavelength is $\lambda = c/f_c$, where c represents the speed of light. For simplicity, we consider time-domain orthogonality, i.e., the transmitters transmit the same signal with relative time shifts. Hence, the received signal components corresponding to various transmitters are readily separated at different receivers. Alternatively, orthogonal waveforms for MIMO-FMCW radars have been designed using beat frequency and chirp rate offsets [39, 40]. In [41], difference co-chirps are proposed for high-accuracy and low complexity range-Doppler estimation in FMCW radars. We consider a CPI of duration $T_p = P_{max}T_c$ corresponding to P_{max} chirps. The standard radar system with full (slow-time) measurements transmits for the entire CPI. In this work, the radar transmits only P out of P_{max} chirps ($P < P_{max}$). We denote the sparse chirp set by $\mathcal{P}_s = \{\zeta_p\}_{1 \leq p \leq P}$ where ζ_p are

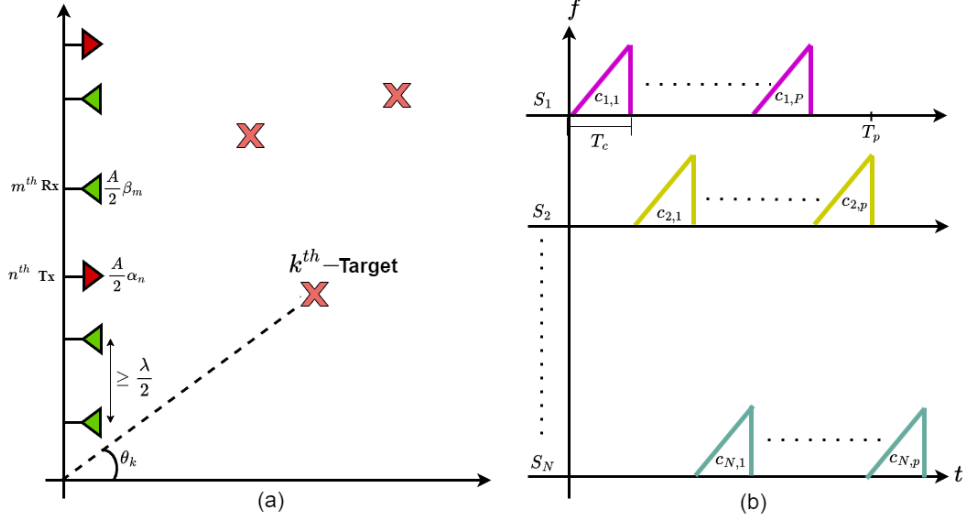


Fig. 1: MIMO-FMCW radar setup with sparse chirps and antenna array: (a) random SLA (green and red triangles denote receivers and transmitters, respectively); and (b) Time-frequency illustration of sparse random chirps transmitted to different angular sectors (S_j and $c_{j,p}$ denote j -th sector and p -th chirp for the j -th sector, respectively).

randomly drawn distinct integers from $\{0, 1, \dots, P_{max} - 1\}$ and distributed as \mathcal{P}_p . On the other hand, in the standard radar, the set $\{\zeta_p\} = \{0, 1, \dots, P_{max} - 1\}$ and the chirps are transmitted in a specific angular sector of interest. In our sparse radar setup, the time corresponding to \mathcal{P}_s^c , i.e., the non-transmitted chirps, can be utilized in other angular sectors, as depicted in Fig. 1b. Throughout the paper, we consider the target's parameter estimation in a single sector only. The received signals from other sectors can be trivially processed in the same manner.

The FMCW radar's LFM chirp transmitted by each transmitter is modeled as

$$s(t) = \exp\left(j2\pi\left(f_c t + \frac{\gamma}{2}t^2\right)\right), \quad 0 \leq t \leq T_c.$$

We consider a target scene of K far-field, non-fluctuating point targets with the k -th target's range, radial velocity, and AOA denoted by R_k , ν_k , and θ_k , respectively. In our proposed framework, the received signal from each transmitted chirp is processed independently at every receiver. Hence, we first focus on the received signal component at the m -th receiver corresponding to the p -th chirp transmitted from n -th transmitter, given by

$$r_{n,m,p}(t) = \sum_{k=1}^K a_k s(t - \tau_{n,m,p}^k), \quad \zeta_p T_c \leq t < (\zeta_p + 1)T_c,$$

where a_k is the complex amplitude proportional to the k -th target's radar cross-section (RCS) and $\tau_{n,m,p}^k$ is the total time-delay in the k -th target's return. The delay $\tau_{n,m,p}^k$ consists of range delay τ_k^R , Doppler delay $\tau_{p,k}^D$ and angular delay $\tau_{n,m,k}^\theta$ as

$$\tau_{n,m,p}^k = \tau_k^R + \tau_{p,k}^D + \tau_{n,m,k}^\theta, \quad (1)$$

where $\tau_k^R = 2R_k/c$, $\tau_{p,k}^D = 2\nu_k \zeta_p T_c / c$ and $\tau_{n,m,k}^\theta = A \sin(\theta_k) \times (\alpha_n + \beta_m) / 2c$. Note that $\tau_{p,k}^D$ represents the additional delay (compared to the range delay) in the target's return because of the target's receding motion in $\zeta_p T_c$ time interval at velocity ν_k . Also, the far-field assumption results in a constant AOA across the array.

At the m -th receiver, the received signal $r_{n,m,p}(t)$ is mixed with the transmitted chirp $s(t)$ to obtain the IF signal as

$$y_{n,m,p}(t) = s(t)r_{n,m,p}^*(t) = \sum_{k=1}^K a_k^* \exp(j2\pi\gamma\tau_{n,m,p}^k t) \times \exp(-j\pi\gamma(\tau_{n,m,p}^k)^2) \exp(j2\pi f_c \tau_{n,m,p}^k t),$$

which is then sampled at sampling frequency f_s to yield the (discrete) fast-time measurements

$$y_{n,m,p}[t] = \sum_{k=1}^K a_k^* \underbrace{\exp\left(j2\pi\gamma\tau_{n,m,p}^k \frac{t}{f_s}\right)}_{\text{Term-I}} \times \underbrace{\exp(-j\pi\gamma(\tau_{n,m,p}^k)^2)}_{\text{Term-II}} \underbrace{\exp(j2\pi f_c \tau_{n,m,p}^k t)}_{\text{Term-III}}. \quad (2)$$

We, henceforth, deal with only discrete-time signals and use t to denote the discrete-time index with $0 \leq t \leq N - 1$ where $N = \lceil f_s T_c \rceil$. In a MIMO-FMCW radar with N_T transmitters, N_R receivers and P chirps, we obtain ' $N_T N_R \times P$ ' sampled measurements $\{y_{n,m,p}[t]\}_{1 \leq n \leq N_T, 1 \leq m \leq N_R, 1 \leq p \leq P}$.

We now show that the target parameter estimation is, in fact, a 3D frequency estimation problem under suitable approximations for practical systems.

Term-I: For practical FMCW radars with narrow-band assumption, we have $\tau_k^R \gg \tau_{p,k}^D$ and $\tau_k^R \gg \tau_{n,m,k}^\theta$ for all targets such that $\gamma\tau_{n,m,p}^k / f_s \approx \gamma\tau_k^R / f_s$. This can also be verified numerically for a radar target with the parameter values provided in Table I. We define the normalized beat frequency (due to range) as $\Omega_R^k \doteq \gamma\tau_k^R / f_s$ and approximate Term-I as $\exp(j2\pi\Omega_R^k t)$. This term is further examined in Section III-B using DFT-based focusing or OMP-recovery methods to obtain the range estimates.

Term-II: Again, using $\tau_k^R \gg \tau_{p,k}^D + \tau_{n,m,k}^\theta$, we have $(\tau_{n,m,p}^k)^2 \approx (\tau_k^R)^2$ [42]. Hence, Term-II becomes $\exp(-j\pi\gamma)(\tau_k^R)^2$, a constant for each target independent of chirp and antenna indices. In the 3D-mixture model (3), we include this term in \tilde{a}_k and is not the focus of the parameter estimation problem addressed in this paper.

Term-III: Substituting (1) in Term-III, we obtain

$$\exp(j2\pi f_c \tau_{n,m,p}^k) = \exp(j2\pi f_c \tau_k^R) \exp\left(j2\pi \frac{2\nu_k T_c}{\lambda} \zeta_p\right) \times \exp\left(j2\pi \frac{A \sin(\theta_k)}{2\lambda} (\alpha_n + \beta_m)\right).$$

Here, $\exp(j2\pi f_c \tau_k^R)$ does not vary with antenna elements and chirps and hence, included in \tilde{a}_k in (3). Define the normalized Doppler frequency $\Omega_D^k \doteq 2\nu_k T_c / \lambda$ and normalized angular/spatial frequency $\Omega_\theta^k \doteq A \sin(\theta_k) / 2\lambda$. Term-III is investigated in Section III-C to jointly estimate the target velocities and AOAs.

With these approximations and including the noise term $w_{n,m,p}[t]$ to represent the interference and noises present in the radar measurements, (2) simplifies to

$$y_{n,m,p}[t] \approx \sum_{k=1}^K \tilde{a}_k^* \exp(j2\pi \Omega_R^k t) \exp(j2\pi \Omega_D^k \zeta_p) \times \exp(j2\pi \Omega_\theta^k (\alpha_n + \beta_m)) + w_{n,m,p}[t], \quad (3)$$

where $\tilde{a}_k = a_k \exp(j\pi \gamma (\tau_k^R)^2) \exp(-j2\pi f_c \tau_k^R)$. Here, (3) consists of a separable mixture of three different complex exponentials such that the target range, velocity, and AOA estimation problem is equivalent to 3D frequency estimation.

Remark 1. The model (3) represents a generalized received IF signal for both full and sparse measurement radars. In particular, in the case of SLA and the sparse chirps, α_n , β_m , and ζ_p are randomly drawn from suitable distributions and represent non-uniform measurements. On the other hand, in conventional radar setups, these quantities correspond to the uniformly placed antenna elements and chirps transmitted over the entire CPI.

III. SPARSE TARGET-PARAMETER RECOVERY

In this section, unlike prior studies, we consider both range and joint Doppler-angle estimation using CS-based methods in Sections III-B and III-C, respectively. As a precursor, Section III-A provides a brief overview of the standard sparse signal recovery problem and the CS framework.

A. CS sparse signal recovery

Consider the linear measurement model

$$\mathbf{y} = \mathbf{A}\mathbf{x} + \mathbf{w}, \quad (4)$$

where $\mathbf{x} \in \mathbb{C}^{N \times 1}$ is the signal measured under the sensing matrix $\mathbf{A} \in \mathbb{C}^{M \times N}$ to yield measurements $\mathbf{y} \in \mathbb{C}^{M \times 1}$, and $\mathbf{w} \in \mathbb{C}^{M \times 1}$ is the additive noise. CS aims to recover a sparse vector \mathbf{x} given a small number of measurements \mathbf{y} with $M \ll N$ such that (4) is an under-determined system. A vector \mathbf{x} is said to be K -sparse if $\|\mathbf{x}\|_0 \leq K < N$. Theoretically, a K -sparse \mathbf{x} can be recovered from (4) for $M \ll N$ by solving the non-convex combinatorial problem

$$\min_{\mathbf{x}} \|\mathbf{x}\|_0 \text{ s.t. } \|\mathbf{y} - \mathbf{A}\mathbf{x}\|_2 \leq \epsilon, \quad (5)$$

where the parameter ϵ is chosen based on the statistics of the noise \mathbf{w} . However, solving (5) is an NP-hard problem and involves an exhaustive search of exponential complexity over all possible combinations of non-zero indices of \mathbf{x} [43]. Hence, approximate solutions of polynomial complexity have been developed in CS.

CS algorithms can be broadly categorized into matching pursuit (MP) and basis pursuit (BP) methods. In MP or greedy methods, new indices are added recursively to the previous provisional support. OMP [44], orthogonal least squares (OLS) [45] and CoSAMP [46] are widely used MP algorithms. On the other hand, BP relaxes the l_0 -norm in (5) to an l_1 -norm [47] resulting in a convex minimization problem for which a globally optimal solution can be obtained in polynomial time. The standard BP and LASSO [48] formulations of (5) are

$$\text{BP: } \min_{\mathbf{x}} \|\mathbf{x}\|_1 \text{ s.t. } \|\mathbf{y} - \mathbf{A}\mathbf{x}\|_2 \leq \epsilon, \quad (6)$$

$$\text{LASSO: } \min_{\mathbf{x}} \|\mathbf{y} - \mathbf{A}\mathbf{x}\|_2 \text{ s.t. } \|\mathbf{x}\|_1 \leq \kappa, \quad (7)$$

where κ is chosen based on the desired sparsity of \mathbf{x} .

The measurement model (4) can be generalized to 2D-separable measurements as

$$\mathbf{Y} = \mathbf{A}\mathbf{X}\mathbf{B}^T + \mathbf{W}, \quad (8)$$

where $\mathbf{X} \in \mathbb{C}^{N_1 \times N_2}$ is the sparse input matrix, $\mathbf{A} \in \mathbb{C}^{M_1 \times N_1}$ and $\mathbf{B} \in \mathbb{C}^{M_2 \times N_2}$ are the measurement matrices, $\mathbf{Y} \in \mathbb{C}^{M_1 \times M_2}$ contains the 2D measurements with $M_1 M_2 \ll N_1 N_2$ and $\mathbf{W} \in \mathbb{C}^{M_1 \times M_2}$ is the noise term. One approach to recover \mathbf{X} is to vectorize the model (8) and then apply standard 1D-MP or BP methods. Alternatively, matrix \mathbf{X} can be recovered directly using matrix projections as in 2D-OMP [49, 50]. We consider both vectorized and 2D-OMP methods to jointly estimate the target velocities and AOAs in Section III-C.

B. Range estimation

We first estimate the target ranges from measurements (3) using two different methods: DFT-based focusing and OMP. The target velocities and AOAs are then jointly estimated for each detected range in the subsequent section.

1) DFT-based focusing: Consider the N -point normalized DFT of (3) across the fast time samples (i.e, t) for the p -th chirp and (n, m) -th virtual array channel as

$$Y_{n,m,p}[l] = \frac{1}{\sqrt{N}} \sum_{t=0}^{N-1} y_{n,m,p}[t] \exp(-j2\pi \frac{lt}{N}) \\ = \sum_{k=1}^K \tilde{a}_k^* \exp(j2\pi \Omega_D^k \zeta_p) \exp(j2\pi \Omega_\theta^k (\alpha_n + \beta_m)) \\ \times \frac{1}{\sqrt{N}} \sum_{t=0}^{N-1} \exp\left(j2\pi \left(\Omega_R^k - \frac{l}{N}\right) t\right) + W_{n,m,p}[l], \quad (9)$$

for $0 \leq l \leq N-1$ and $W_{n,m,p}[l] = (1/\sqrt{N}) \sum_{t=0}^{N-1} w_{n,m,p}[t] \exp(-j2\pi lt/N)$.

Now, we can approximate the sum of M exponents $g(x|\bar{x}) = \frac{1}{\sqrt{M}} \sum_{q=0}^{M-1} e^{j(x-\bar{x})q\omega}$ for given constants \bar{x} and ω as

$$|g(x|\bar{x})| \approx \begin{cases} \sqrt{M}, & |x - \bar{x}| \leq \pi/M\omega \\ 0, & |x - \bar{x}| > \pi/M\omega \end{cases}$$

This approximation implies that in the focus zone $|x - \bar{x}| \leq \pi/M\omega$, the M exponents are coherently integrated while the signal outside the focus zone is severely attenuated. This focusing operation was applied across pulses in [26] to reduce the joint delay-Doppler estimation problem to delay-only estimation in a pulsed-Doppler radar. In our range estimation, the sum of exponents appears naturally in the IF signal's DFT in (9).

Using the focusing approximation for the sum $\frac{1}{\sqrt{N}} \sum_{t=0}^{N-1} \exp(j2\pi (\Omega_R^k - \frac{l}{N}) t)$ in (9), we have

$$Y_{n,m,p}[l] = \sum_{k'=1}^{K'} \tilde{a}_{k'}^* \sqrt{N} \exp(j2\pi \Omega_D^{k'} \zeta_p) \exp(j2\pi \Omega_\theta^{k'} (\alpha_n + \beta_m)) \\ + W_{n,m,p}[l], \quad (10)$$

where $\{\tilde{a}_{k'}, \Omega_R^{k'}, \Omega_D^{k'}, \Omega_\theta^{k'}\}_{1 \leq k' \leq K'}$ represents the subset of K' target's that satisfy $|\Omega_R^{k'} - l/N| \leq 1/2N$, i.e., K' targets are present in l -th range bin. Substituting $N = f_s T_c$ and $\Omega_R^{k'} = \gamma \tau_{k'}^R / f_s$, the condition $|\Omega_R^{k'} - l/N| \leq 1/2N$ simplifies to $|\tau_{k'}^R - l/\gamma T_c| \leq 1/2\gamma T_c$. Furthermore, for practical FMCW radar systems, $1/2\gamma T_c$ is small such that

$$\tau_{k'}^R \approx l/\gamma T_c. \quad (11)$$

The target returns with range delay (11) are coherently integrated and result in a (magnitude) peak at the l -th DFT bin. We can identify these peaks in $Y_{n,m,p}[l]$ using threshold detection and obtain the range estimate corresponding to l' -th detected bin as $R' = cl'/2\gamma T_c$.

Binary integration: So far, we have considered range estimation from a given p -th chirp and (n, m) -th virtual array channel. Similarly, the range estimates are computed independently for all P chirps and $N_T N_R$ channels using the radar measurements $\{y_{n,m,p}[t]\}_{1 \leq n \leq N_T, 1 \leq m \leq N_R, 1 \leq p \leq P}$. In binary integration, these detected ranges are then filtered for false alarms and missed detections across all chirps and channels using a majority rule, i.e., only the ranges detected in the majority of measurements are considered valid.

Remark 2 (Coherent and binary integration). *Classical-DFT range processing also involves peak detection in the DFT of the sampled IF signal. However, in classical processing, the measurements from all chirps and array channels are processed coherently to average out the noise term. However, at low SNRs, the method fails to detect range bins where the noise is significant. Contrarily, in binary integration, a missed range in one measurement can be detected in other measurements, reducing the missed detection probability, as demonstrated in Section V-A. However, our joint Doppler-angle estimation procedure proposed later can also be trivially applied to coherently processed measurements.*

2) Range-OMP: In (11), the range resolution is $c/2\gamma T_c$ where γT_c is the total bandwidth swept by the LFM chirp. This resolution is the same as the classical-DFT [10], which requires large bandwidth and heavy computation. To this end, we propose an alternative OMP-based range recovery method.

Consider the measurements $y_{1,1,1}[t]$ from the first chirp and the first virtual array channel. Denote $x_k \doteq \tilde{a}_k^* \exp(j2\pi\Omega_D^k \zeta_p) \exp(j2\pi\Omega_\theta^k (\alpha_n + \beta_m))$ and stack the samples $y_{1,1,1}[t]$ for $0 \leq t \leq N-1$ in a $N \times 1$ vector \mathbf{y}_R . Now, define the $K \times 1$ vector $\tilde{\mathbf{x}}_R = [x_1, \dots, x_K]^T$ such that (3) yields

$$\mathbf{y}_R = \tilde{\mathbf{A}}(\Omega_R) \tilde{\mathbf{x}}_R + \mathbf{w}_R, \quad (12)$$

where the $N \times K$ matrix $\tilde{\mathbf{A}}(\Omega_R) = [\mathbf{a}(\Omega_R^1), \dots, \mathbf{a}(\Omega_R^K)]$ with the k -th column $\mathbf{a}(\Omega_R^k) \doteq [1, \exp(j2\pi\Omega_R^k), \dots, \exp(j2\pi\Omega_R^k(N-1))]^T$. Here, \mathbf{w}_R represents the $N \times 1$ stacked noise vector. Each column $\mathbf{a}(\Omega_R)$ of matrix $\tilde{\mathbf{A}}$ is parameterized by the (range) beat frequency Ω_R and is equivalent to steering vector in the beat frequency domain. Furthermore, \mathbf{y}_R in (12) represents full measurements in the fast-time domain sampled at frequency f_s .

We choose a grid of G_R points $\{\omega_g : 1 \leq g \leq G_R\}$ of the possible target beat frequencies Ω_R (or equivalently ranges) with $G_R \gg K$ and negligible discretization errors. Substituting these grid points in $\mathbf{a}(\cdot)$, we construct an over-complete $N \times G_R$ measurement matrix $\mathbf{A} = [\mathbf{a}(\omega_1), \dots, \mathbf{a}(\omega_{G_R})]$. Then, (12) becomes

$$\mathbf{y}_R = \mathbf{A} \mathbf{x}_R + \mathbf{w}_R, \quad (13)$$

where the $G_R \times 1$ vector \mathbf{x}_R contains the target ranges and unknown coefficients $\{x_k\}$. In particular, a non-zero element of \mathbf{x}_R represents a target present at the range corresponding to the grid point. Since $K \ll G_R$, \mathbf{x}_R is a sparse vector and range estimation reduces to determining $\text{supp}(\mathbf{x}_R)$ given \mathbf{y}_R and \mathbf{A} . To this end, we can employ any 1D-MP or BP recovery algorithms described in Section III-A. In particular, we use OMP in Section V.

Remark 3 (Range-OMP and DFT-focusing). *Range-OMP in (13) considers measurements only from one chirp and one array channel. This is in contrast to DFT-focusing, wherein all the measurements are integrated (binary or coherently) to obtain valid target ranges making them computationally expensive. Furthermore, range-OMP provides superior range resolution compared to DFT-focusing, determined by the choice of grid $\omega_{1 \leq g \leq G_R}$ and not by parameters γ and T_c . However, the $\text{supp}(\mathbf{x}_R)$'s recovery still depends on the matrix \mathbf{A} such that the recovery probability is low if the grid points are too close.*

C. Joint Doppler-angle estimation

Consider a range detected at the l' -th DFT bin while the corresponding DFT coefficients $Y_{n,m,p}[l']$ are given by (10) for $1 \leq p \leq P$, $1 \leq n \leq N_T$ and $1 \leq m \leq N_R$. The following joint Doppler-angle estimation method processes DFT measurements given by (10) at a particular range bin. In the range-OMP case, the target ranges are estimated at a higher resolution grid $\omega_{1 \leq g \leq G_R}$, but then converted to the associated DFT bin and the measurements $Y_{n,m,p}[l']$ are computed. At the l' -th range bin, we assume that K' targets are present such that

$$Y_{n,m,p}[l'] = \sum_{k'=1}^{K'} \tilde{a}_{k'}^* \sqrt{N} \exp(j2\pi\Omega_D^{k'} \zeta_p) \exp(j2\pi\Omega_\theta^{k'} (\alpha_n + \beta_m)) + W_{n,m,p}[l']. \quad (14)$$

Note that the exponential terms with the Doppler and angular frequencies are separable in $Y_{n,m,p}[l']$.

We stack the measurements $Y_{n,m,p}[l']$ for all $1 \leq n \leq N_T$ and $1 \leq m \leq N_R$ in a $N_T N_R \times 1$ vector \mathbf{y}_p for the p -th chirp. Further, define the $N_T N_R \times P$ matrix $\mathbf{Y} = [\mathbf{y}_1, \dots, \mathbf{y}_P]$ and the steering vectors in the Doppler and angular frequency domains as $\mathbf{b}(\Omega_D)$ and $\mathbf{c}(\Omega_\theta)$, respectively, as

$$\begin{aligned} \mathbf{b}(\Omega_D) &\doteq [\exp(j2\pi\Omega_D \zeta_1), \dots, \exp(j2\pi\Omega_D \zeta_P)]^T, \\ \mathbf{c}(\Omega_\theta) &\doteq [\exp(j2\pi\Omega_\theta (\alpha_1 + \beta_1)), \dots, \exp(j2\pi\Omega_\theta (\alpha_{N_T} + \beta_{N_R}))]^T. \end{aligned} \quad (15)$$

Similarly, we define the $K' \times K'$ matrix $\tilde{\mathbf{Z}} \doteq \text{diag}(z_1, z_2, \dots, z_{K'})$ where $z_{k'} = \tilde{a}_{k'}^* \sqrt{N}$. Then, using (14), we obtain

$$\mathbf{Y} = \tilde{\mathbf{C}}(\Omega_\theta) \tilde{\mathbf{Z}} \tilde{\mathbf{B}}^T(\Omega_D) + \mathbf{W}, \quad (17)$$

where the $N_T N_R \times K'$ matrix $\tilde{\mathbf{C}}(\Omega_\theta) = [\mathbf{c}(\Omega_\theta^1), \dots, \mathbf{c}(\Omega_\theta^{K'})]$ and the $P \times K'$ matrix $\tilde{\mathbf{B}}(\Omega_D) = [\mathbf{b}(\Omega_D^1), \dots, \mathbf{b}(\Omega_D^{K'})]$. Again, \mathbf{W} represents the $N_T N_R \times P$ stacked noise matrix.

Our goal is to recover $\Omega_\theta = \{\Omega_\theta^1, \dots, \Omega_\theta^{K'}\}$ and $\Omega_D = \{\Omega_D^1, \dots, \Omega_D^{K'}\}$ from \mathbf{Y} with a small number of transmitted chirps and antenna elements. To this end, we exploit the sparseness of the target scene. We choose grids of G_D points $\rho_{1 \leq g \leq G_D}$ and G_θ points $\phi_{1 \leq g \leq G_\theta}$ of the possible target Doppler and angular frequencies, respectively, with both $G_D, G_\theta \gg K$ and negligible discretization errors. Note that from $\Omega_D = 2\nu T_c / \lambda$ and $\Omega_\theta = A \sin(\theta) / 2\lambda$, the grids $\rho_{1 \leq g \leq G_D}$ and $\phi_{1 \leq g \leq G_\theta}$ are equivalently defined on possible target velocities and AOAs, respectively. Substituting these grid points in $\mathbf{b}(\cdot)$ and $\mathbf{c}(\cdot)$, we construct the $P \times G_D$ measurement matrix $\mathbf{B} = [\mathbf{b}(\rho_1), \dots, \mathbf{b}(\rho_{G_D})]$ and the $N_T N_R \times G_\theta$ measurement matrix $\mathbf{C} = [\mathbf{c}(\phi_1), \dots, \mathbf{c}(\phi_{G_\theta})]$. Finally, (17) can be expressed as

$$\mathbf{Y} = \mathbf{C} \mathbf{Z} \mathbf{B}^T + \mathbf{W}, \quad (18)$$

where the unknown $G_\theta \times G_D$ matrix \mathbf{Z} contains the coefficients $\{z_{k'}\}$ as well as the target velocities and AOAs information. Particularly, a non-zero element in \mathbf{Z} represents a target with its AOA and velocity equal to that of the corresponding point in the 2D grid $\{(\phi_{i_1}, \rho_{i_2}) : 1 \leq i_1 \leq G_\theta, 1 \leq i_2 \leq G_D\}$. Since $K' \ll G_D G_\theta$, the matrix \mathbf{Z} is sparse, and hence, the desired velocities and AOAs can be recovered using small number of measurements \mathbf{Y} given matrices \mathbf{C} and \mathbf{B} . Note that the joint Doppler-angle estimation has now been reduced to determining $\text{supp}(\mathbf{Z})$. In (18), the measurement matrices \mathbf{C} and \mathbf{B} and hence, the recovery guarantees depend on the choice of grids $\rho_{1 \leq g \leq G_D}$ and $\phi_{1 \leq g \leq G_\theta}$ as well as the number and (random) locations of the transmitted chirps ($\zeta_{1 \leq p \leq P}$) and antenna elements ($\alpha_{1 \leq n \leq N_T}$ and $\beta_{1 \leq m \leq N_R}$).

Recall that the 2D sparse recovery problem (18) can be solved using either 1D vectorized CS or direct 2D-OMP methods. For the

vectorized method, we denote $\mathbf{y} = \text{vec}(\mathbf{Y})$, $\mathbf{z} = \text{vec}(\mathbf{Z})$, $\mathbf{w} = \text{vec}(\mathbf{W})$ and $\mathbf{D} = \mathbf{B} \otimes \mathbf{C}$. The equivalent 1D sparse recovery model of (18) is then

$$\mathbf{y} = \mathbf{D}\mathbf{z} + \mathbf{w}, \quad (19)$$

which is same as (4) with \mathbf{A} and \mathbf{x} replaced by \mathbf{D} and \mathbf{z} , respectively. In Section IV, we consider the l_1 -minimization-based solution of (19) to derive the theoretical recovery guarantees while Section V numerically compares both 2D-OMP and vectorized CS methods.

IV. RECOVERY GUARANTEES

As mentioned in Section III-A, the l_1 -minimization formulations are relaxations of the original CS recovery problem. Hence, the solutions obtained from (6) or (7) can be different from that of (5). To this end, sufficient conditions to guarantee correct recovery through l_1 minimization methods are extensively studied [43, 51–53]. In this context, two kinds of recovery guarantees are defined:

1) Uniform recovery: Uniform recovery means that for a fixed instantiation of the random measurement matrix \mathbf{D} , all possible K -sparse vectors \mathbf{z} are recovered with high probability. Uniform recovery is guaranteed if \mathbf{D} satisfies the restricted isometry property (RIP) with high probability [43]. Furthermore, if the mutual coherence μ of matrix \mathbf{D} is small, then \mathbf{D} satisfies RIP where

$$\mu \doteq \max_{i \neq l} \frac{|\mathbf{D}_{:,i}^H \mathbf{D}_{:,l}|}{\|\mathbf{D}_{:,i}\|_2 \|\mathbf{D}_{:,l}\|_2} \quad (20)$$

2) Non-uniform recovery: Consider a given K -sparse vector \mathbf{z}_s and a measurement matrix \mathbf{D} drawn at random independent of \mathbf{z}_s . Non-uniform recovery guarantees provide conditions under which \mathbf{z}_s is recovered with high probability. Non-uniform recovery follows if \mathbf{D} satisfies isotropy property with high probability [54], i.e., the components of each row of \mathbf{D} have unit variance and are uncorrelated such that for every i ,

$$\mathbb{E}[\mathbf{D}_{i,:}^H \mathbf{D}_{i,:}] = \mathbf{I}. \quad (21)$$

Note that uniform recovery implies non-uniform recovery, but the converse is not true.

In the following, we consider our sparse chirps and SLA radar setup, described in Section II, and derive sufficient conditions for both uniform and non-uniform recovery for the vectorized joint Doppler-angle estimation problem (19). Particularly, we provide sufficient conditions on distributions (\mathcal{P}_p , \mathcal{P}_α and \mathcal{P}_β), number of chirps and antenna elements (P , N_T and N_R), and grids ($\rho_{1 \leq g \leq G_D}$ and $\phi_{1 \leq g \leq G_\theta}$) such that the RIP and isotropy properties are satisfied with high probability. Section IV-C then discusses practical distribution and grid choices that satisfy these conditions.

Consider the vectorized model (19). Since $\mathbf{D} = \mathbf{B} \otimes \mathbf{C}$, any column of \mathbf{D} is represented as $\mathbf{D}_{:,G_\theta(i_1-1)+i_2} = \mathbf{B}_{:,i_1} \otimes \mathbf{C}_{:,i_2}$ where $1 \leq i_1 \leq G_D$ and $1 \leq i_2 \leq G_\theta$. Similarly, any row of \mathbf{D} is represented by $\mathbf{D}_{N_T N_R(i_1-1)+i_2,:} = \mathbf{B}_{i_1,:} \otimes \mathbf{C}_{i_2,:}$ where $1 \leq i_1 \leq P$ and $1 \leq i_2 \leq N_T N_R$. Further, consider a Doppler grid point ρ_i . Substituting $\Omega_D = 2\nu T_c / \lambda$ in (15), we obtain the i -th column of matrix \mathbf{B} corresponding to ρ_i as $\mathbf{b}(\rho_i) = [\exp(j \frac{4\pi T_c}{\lambda} \rho_i \zeta_1), \dots, \exp(j \frac{4\pi T_c}{\lambda} \rho_i \zeta_P)]^T$. Similarly, substituting $\Omega_\theta = A \sin \theta / 2\lambda$ in (16), we obtain the i -th column of matrix \mathbf{C} corresponding to angular grid point ϕ_i as $\mathbf{c}(\phi_i) = [\exp(j \frac{\pi A}{\lambda} \sin \phi_i (\alpha_1 + \beta_1)), \dots, \exp(j \frac{\pi A}{\lambda} \sin \phi_i (\alpha_{N_T} + \beta_{N_R}))]^T$. Define $\mathbf{Q}_D \doteq \mathbf{D}^H \mathbf{D}$, $\mathbf{Q}_B \doteq \mathbf{B}^H \mathbf{B}$ and $\mathbf{Q}_C \doteq \mathbf{C}^H \mathbf{C}$. From (20) and (21), we observe that the RIP and isotropy conditions for measurement matrix \mathbf{D} are closely related to the statistics of matrix \mathbf{Q}_D . In particular, coherence μ is the maximum absolute value among normalized off-diagonal elements of \mathbf{Q}_D while $\mathbb{E}[\mathbf{D}_{i,:}^H \mathbf{D}_{l,:}] =$

$(1/P N_T N_R) \mathbb{E}[\mathbf{Q}_D]$ such that (21) implies $\mathbb{E}[\mathbf{Q}_D] = P N_T N_R \mathbf{I}$. Also, we can trivially show that $\mathbf{Q}_D = \mathbf{Q}_B \otimes \mathbf{Q}_C$. For simplicity, denote $u_{i_1, i_2}^D = \frac{4\pi T_c}{\lambda} (\rho_{i_2} - \rho_{i_1})$ and $u_{i_1, i_2}^\theta = \frac{\pi A}{\lambda} (\sin \phi_{i_2} - \sin \phi_{i_1})$. We define

$$\begin{aligned} \Gamma_B(u_{i_1, i_2}^D) &\doteq \frac{\mathbf{B}_{:,i_1}^H \mathbf{B}_{:,i_2}}{\|\mathbf{B}_{:,i_1}\|_2 \|\mathbf{B}_{:,i_2}\|_2} = \frac{1}{P} \sum_{p=1}^P \exp(j u_{i_1, i_2}^D \zeta_p), \quad (22) \\ \Gamma_C(u_{i_1, i_2}^\theta) &\doteq \frac{\mathbf{C}_{:,i_1}^H \mathbf{C}_{:,i_2}}{\|\mathbf{C}_{:,i_1}\|_2 \|\mathbf{C}_{:,i_2}\|_2} \\ &= \frac{1}{N_T N_R} \sum_{n=1}^{N_T} \sum_{m=1}^{N_R} \exp(j u_{i_1, i_2}^\theta (\alpha_n + \beta_m)). \quad (23) \end{aligned}$$

Note that both $\Gamma_B(\cdot)$ and $\Gamma_C(\cdot)$ are random variables because of the randomly drawn transmitter and receiver locations (via α_n and β_m) and the randomly transmitted chirps (via ζ_p).

A. Uniform recovery

Consider the coherence of matrix \mathbf{D} given as

$$\begin{aligned} \mu &= \max_{l_1 \neq l_2} \frac{|\mathbf{D}_{:,l_1}^H \mathbf{D}_{:,l_2}|}{\|\mathbf{D}_{:,l_1}\|_2 \|\mathbf{D}_{:,l_2}\|_2} \\ &= \max_{(i_1, j_1) \neq (i_2, j_2)} \frac{|\mathbf{D}_{:,G_\theta(i_1-1)+j_1}^H \mathbf{D}_{:,G_\theta(i_2-1)+j_2}|}{\|\mathbf{D}_{:,G_\theta(i_1-1)+j_1}\|_2 \|\mathbf{D}_{:,G_\theta(i_2-1)+j_2}\|_2}. \end{aligned}$$

Substituting $\mathbf{D}_{:,G_\theta(i-1)+j} = \mathbf{B}_{:,i} \otimes \mathbf{C}_{:,j}$, we obtain

$$\begin{aligned} \mu &= \max_{\{(i_1, j_1) \neq (i_2, j_2)\}} \frac{|\mathbf{B}_{:,i_1}^H \mathbf{B}_{:,i_2}|}{\|\mathbf{B}_{:,i_1}\|_2 \|\mathbf{B}_{:,i_2}\|_2} \times \frac{|\mathbf{C}_{:,j_1}^H \mathbf{C}_{:,j_2}|}{\|\mathbf{C}_{:,j_1}\|_2 \|\mathbf{C}_{:,j_2}\|_2}, \\ &= \max_{\{(i_1, j_1) \neq (i_2, j_2)\}} |\Gamma_B(u_{i_1, i_2}^D)| \times |\Gamma_C(u_{j_1, j_2}^\theta)| \end{aligned}$$

Now, $\max_{(i_1, j_1) \neq (i_2, j_2)} (\cdot) = \max_{\{i_1 \neq i_2\} \cup \{j_1 \neq j_2\}} (\cdot) = \max\{\max_{i_1 \neq i_2} (\cdot), \max_{j_1 \neq j_2} (\cdot)\}$. Furthermore, $|\Gamma_C(u_{j_1, j_2}^\theta)| \leq 1$ such that $\max_{i_1 \neq i_2} |\Gamma_B(u_{i_1, i_2}^D)| \times |\Gamma_C(u_{j_1, j_2}^\theta)| \leq \max_{i_1 \neq i_2} |\Gamma_B(u_{i_1, i_2}^D)|$. Similarly, $\max_{j_1 \neq j_2} |\Gamma_B(u_{i_1, i_2}^D)| \times |\Gamma_C(u_{j_1, j_2}^\theta)| \leq \max_{j_1 \neq j_2} |\Gamma_C(u_{j_1, j_2}^\theta)|$. Hence,

$$\mu \leq \max\{\max_{i_1 \neq i_2} |\Gamma_B(u_{i_1, i_2}^D)|, \max_{j_1 \neq j_2} |\Gamma_C(u_{j_1, j_2}^\theta)|\} \quad (24)$$

Lemma 1. *If $\rho_{1:G_D}$ is a uniform grid of Doppler frequencies, then matrix $\mathbf{Q}_B = \mathbf{B}^H \mathbf{B}$ is a Toeplitz matrix with all main diagonal elements equal to P . Similarly, if $\phi_{1:G_\theta}$ is an angular grid uniform in $\sin \theta$ domain, then $\mathbf{Q}_C = \mathbf{C}^H \mathbf{C}$ is a Toeplitz matrix with all main diagonal elements equal to $N_T N_R$.*

Proof: See Appendix A. ■

By the virtue of Lemma 1, for uniform grids, the statistics of $\Gamma_B(\cdot)$ and $\Gamma_C(\cdot)$ (and consequently μ) are characterized by considering only the first rows of \mathbf{Q}_B and \mathbf{Q}_C , respectively, i.e., $\mathbf{B}_{:,i_1}^H \mathbf{B}_{:,i_1}$ for $i_1 = 2, 3, \dots, G_D$ and $\mathbf{C}_{:,i_2}^H \mathbf{C}_{:,i_2}$ for $i_2 = 2, 3, \dots, G_\theta$. Note that $\|\mathbf{B}_{:,i_1}\|_2 = \sqrt{P}$ for all i_1 and $\|\mathbf{C}_{:,i_2}\|_2 = \sqrt{N_T N_R}$ for all i_2 .

In the following, we address two cases: (a) N_T transmitters and N_R receivers, where $\alpha_{1:N_T}$ and $\beta_{1:N_R}$ are independent, and (b) $N_T = N_R$ transceivers, where $\alpha_n = \beta_n$ for all $1 \leq n \leq N_T$. Theorem 1 upper bounds the complementary cdf of μ for both these cases.

Theorem 1 (Coherence of measurement matrix \mathbf{D}). *Consider the random sparse chirps and SLA radar setup of Section II wherein the transmitters' positions $\alpha_{1:N_T}$ and receivers' positions $\beta_{1:N_R}$ are drawn i.i.d. from even distributions \mathcal{P}_α and \mathcal{P}_β , respectively. The chirps' indices $\zeta_{1:P} \in \{0, 1, \dots, P_{\max} - 1\}$ are distinct and distributed as \mathcal{P}_p , which is symmetrical about $(P_{\max} - 1)/2$. The Doppler grid $\rho_{1:G_D}$ and angular grid $\phi_{1:G_\theta}$ are uniform in the velocity and $\sin \theta$ domains, respectively. Let the following assumptions*

¹trivially proved taking element-wise expectations and comparing matrix elements on both sides.

hold true.

C1. Distribution \mathcal{P}_p and grid $\rho_{1:G_D}$ satisfy

$$\Psi_p(u_{1,i}^D) = \Psi_p(2u_{1,i}^D) = 0, \quad (25)$$

for $i = 2, 3, \dots, G_D$ where $\Psi_p(\cdot)$ denotes the characteristic function of \mathcal{P}_p .

C2. Distributions \mathcal{P}_α , \mathcal{P}_β and grid $\phi_{1:G_\theta}$ satisfy

$$\Psi_\alpha(u_{1,i}^\theta) = \Psi_\alpha(2u_{1,i}^\theta) = \Psi_\beta(u_{1,i}^\theta) = \Psi_\beta(2u_{1,i}^\theta) = 0, \quad (26)$$

for $i = 2, 3, \dots, G_\theta$ where $\Psi_\alpha(\cdot)$ and $\Psi_\beta(\cdot)$ denote the characteristic functions of \mathcal{P}_α and \mathcal{P}_β , respectively.

Then, for $0 < \vartheta < 1$, the coherence μ of matrix \mathbf{D} in (19) satisfies the following:

1) If $\alpha_{1:N_T}$ and $\beta_{1:N_R}$ are independent, then

$$\mathbb{P}(\mu > \vartheta) < 1 - (1 - e^{-\vartheta^2 P})^{G_D - 1} \times (1 - 2\vartheta\sqrt{N_T N_R} \mathcal{K}_1(2\vartheta\sqrt{N_T N_R}))^{G_\theta - 1}, \quad (27)$$

where $\mathcal{K}_1(\cdot)$ denotes the modified Bessel function of second kind.

2) For the $N_T = N_R$ transceivers case, $\alpha_n = \beta_n$ for all $1 \leq n \leq N_T$ and

$$\mathbb{P}(\mu > \vartheta) \leq 1 - (1 - e^{-\vartheta^2 P})^{G_D - 1} (1 - e^{-N_T \vartheta})^{G_\theta - 1}. \quad (28)$$

Proof: See Appendix B. ■

Using Theorem 1, we can lower-bound the number of chirps P and antenna elements $N_T N_R$ needed to ensure uniform recovery with high probability as follows.

Theorem 2 (Uniform recovery guarantee). *Consider the random sparse chirps and SLA radar setup with the distributions \mathcal{P}_α , \mathcal{P}_β and \mathcal{P}_p and grids $\rho_{1:G_D}$ and $\phi_{1:G_\theta}$ satisfying the conditions of Theorem 1. Also, consider some $0 < \epsilon < 1$ and two positive constants ϵ_1 and ϵ_2 such that $\epsilon_1 + \epsilon_2 = \epsilon$ and*

$$P \geq \kappa_1 \left(K - \frac{1}{2} \right)^2 \log \left(\frac{G_D}{\epsilon_1} \right), \quad (29)$$

and

$$N_T N_R \geq \kappa_2 \left(K - \frac{1}{2} \right)^2 \left(\log \left(\frac{G_\theta \sqrt{\pi}}{2\epsilon_2} \right) + \frac{1}{2} \log \left(2 \log \left(\frac{G_\theta \sqrt{\pi}}{2\epsilon_2} \right) \right) \right)^2, \quad (30)$$

when $\alpha_{1:N_T}$ and $\beta_{1:N_R}$ are independent, or

$$N_T \geq \kappa_3 \left(K - \frac{1}{2} \right) \log \left(\frac{G_\theta}{\epsilon_2} \right), \quad (31)$$

when $\alpha_n = \beta_n$ for all $1 \leq n \leq N_T$. Here, constants $\kappa_1 \approx 18.69$, $\kappa_2 \approx 4.67$ and $\kappa_3 \approx 4.32$ while K is the maximum number of targets present in a range bin. Then, for any K -sparse \mathbf{z} measured by (19) with $\|\mathbf{w}\|_2 \leq \sigma$, the l_1 -minimization solution $\hat{\mathbf{z}}$ satisfies $\|\hat{\mathbf{z}} - \mathbf{z}\|_2 \leq \kappa_4 \sigma$ with probability at least $1 - \epsilon$, where κ_4 is a constant depending only on the RIP constant δ_{2K} of matrix \mathbf{D} .

Proof: See Appendix C. ■

Theorem 2 guarantees the exact recovery of any K -sparse signal in the noise-free $\sigma = 0$ case with high probability. Note that various possible choices of ϵ_1 and ϵ_2 in (29)-(31) ensure that the number of chirps P and antenna elements $N_T N_R$ can be flexibly adjusted to guarantee joint recovery of target velocities and AOAs. Additionally, $\Gamma_C(\cdot)$ in (23) is closely related to the array pattern of our random SLA [31, 55] such that the bounds in (30) and (31) signify the number of antenna elements necessary to control the peak sidelobes. Note that, similar to [31, 56], the results in Theorems 1-2 are valid for sufficiently large measurements (due to the approximations made in their proofs) and primarily highlight the interdependence

among measurements, grid points, and the number of targets for uniform recovery. However, uniform recovery investigates the worst-case scenario, but the average performance in practice is much better than predicted by Theorem 2. Particularly, in our parameter estimation problem, we are more interested in recovering $\text{supp}(\mathbf{z})$ than the (exact) non-zero values in \mathbf{z} .

Remark 4 (Dependence on number of targets). *From (29), we observe that the number of chirps P may increase quadratically with the number of targets K expected to be present in a range bin. The number of antenna elements ($N_T N_R$ in (30) or N_T in (31)) have a quadratic and linear dependence on K , respectively, for the independent transmitter-receiver and transceivers cases.*

Remark 5 (Dependence on grid points). *In Theorem 2, both the number of chirps P and antenna elements ($N_T N_R$ or N_T) increase logarithmically with the associated number of grid points (G_D or G_θ). This logarithmic dependence signifies that our proposed method enables high-resolution Doppler-angle estimation using only a small number of chirps and antenna elements. On the contrary, for traditional full MIMO radar arrays that transmit chirps for the entire CPI, the angular and velocity resolution depend, respectively, on the array aperture and CPI such that both the chirps and antenna elements scale linearly with grid points for high resolution. However, in our case, grid points G_D and G_θ are not free variables because they need to satisfy (25) and (26), respectively.*

B. Non-uniform recovery

We now examine the isotropy condition (21) for matrix \mathbf{D} and non-uniform guarantees. Recall that any row of \mathbf{D} is represented as $\mathbf{D}_{N_T N_R(i_1-1)+i_2,:} = \mathbf{B}_{i_1,:} \otimes \mathbf{C}_{i_2,:}$ where $1 \leq i_1 \leq P$, $1 \leq i_2 \leq N_T N_R$. Now, any row of matrix \mathbf{C} is $[\exp(j \frac{\pi A}{\lambda} \sin \phi_1 (\alpha_n + \beta_m)), \dots, \exp(j \frac{\pi A}{\lambda} \sin \phi_{G_\theta} (\alpha_n + \beta_m))]$ for some $1 \leq n \leq N_T$ and $1 \leq m \leq N_R$. Hence, rows of \mathbf{C} and, consequently, \mathbf{D} are generally not independent. Non-uniform recovery for such cases has been addressed in [53]. Here, we first provide conditions to satisfy the isotropy property in Theorem 3. The non-uniform recovery guarantees then follow in Theorem 4.

Theorem 3 (Isotropy property for matrix \mathbf{D}). *Consider the random sparse chirps and SLA setup of Theorem 1. Define random variable $\xi = \alpha + \beta$. The matrix \mathbf{D} in (19) satisfies $\mathbb{E}[\mathbf{D}_{i,:}^H \mathbf{D}_{l,:}] = \mathbf{I}$ for every $1 \leq l \leq P N_T N_R$ (isotropy property) iff the distributions \mathcal{P}_p , \mathcal{P}_α and \mathcal{P}_β , and uniform grids $\rho_{1:G_D}$ and $\phi_{1:G_\theta}$ satisfy*

$$\Psi_p(u_{1,i}^D) = 0, \quad \text{and} \quad \Psi_\xi(u_{1,j}^\theta) = 0, \quad (32)$$

for $i = 2, 3, \dots, G_D$ and $j = 2, 3, \dots, G_\theta$, where $\Psi_\xi(\cdot)$ denotes the characteristic function of ξ .

Proof: See Appendix D. ■

Theorem 4 (Non-uniform recovery guarantee). *Consider the random sparse chirps and SLA setup of Theorem 1. Also, consider a given K -sparse signal \mathbf{z} measured by (19) with $\|\mathbf{w}\|_2 \leq \sigma$. We assume that the distributions \mathcal{P}_p , \mathcal{P}_α and \mathcal{P}_β and uniform grids $\rho_{1:G_D}$ and $\phi_{1:G_\theta}$ satisfy (32). Consider some $0 < \epsilon < 1$ such that*

$$P N_T N_R \geq \kappa_5 K \log^2 \left(\frac{\kappa_6 G_D G_\theta}{\epsilon} \right) \quad (33)$$

where $\kappa_5 \leq 2.87 \times 10^6$ and $\kappa_6 \leq 6$ are universal constants while K denotes the maximum number of targets in a range bin. Then, the l_1 minimization solution $\hat{\mathbf{z}}$ satisfies

$$\|\hat{\mathbf{z}} - \mathbf{z}\|_2 \leq \kappa_7 \sigma \sqrt{\frac{K}{P N_T N_R}} \quad (34)$$

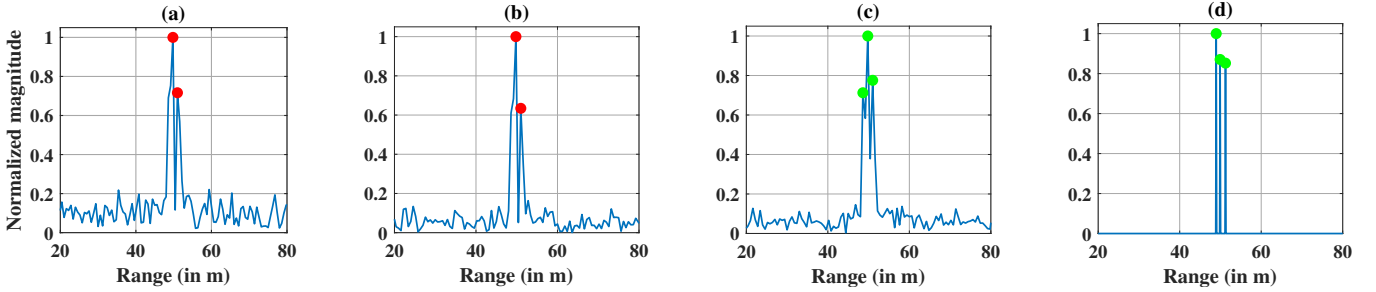


Fig. 2: Range channels for DFT with (a) coherent integration, and (b) Channel-A ($y_{1,1,5}$) and (c) Channel-B ($y_{2,2,6}$) for binary integration; and (d) range-OMP.

with probability at least $1 - \epsilon$, where constant $\kappa_7 \leq 23.513$.

Proof: Using the isotropy property, the non-uniform recovery of K -targets can be guaranteed by generalizing [53, Theorem 2.1] for the vectorized model (19). Particularly, we consider the exact K -sparse signal \mathbf{z} and substitute the following: (a) number of rows of measurement matrix by $PN_T N_R$, (b) sparsity by K , and (c) number of columns of measurement matrix by $G_D G_\theta$. ■

Remark 6 (Uniform and non-uniform recovery). *Contrary to Theorem 2, in non-uniform recovery, the total number of measurements $PN_T N_R$ scales linearly with number of targets K and as $\log^2(G_D G_\theta)$ with the number of grid points. The inequality (33) indicates that the number of chirps P and antenna elements $N_T N_R$ can be flexibly adjusted to obtain high resolutions jointly in Doppler and AOA domains. Note that G_D and G_θ are still not free variables since they need to satisfy (32). However, unlike Theorem 2 where the error does not depend on the number of measurements, R.H.S of (34) in non-uniform recovery is an explicit function of $PN_T N_R$. Again, Theorem 4 guarantees exact recovery for the noise-free $\sigma = 0$ case.*

C. Practical example

Proposition 5 provides a practical example of distributions \mathcal{P}_p , \mathcal{P}_α and \mathcal{P}_β and grids $\rho_{1:G_D}$ and $\phi_{1:G_\theta}$ that satisfy (25)-(26).

Proposition 5. *Consider $A_T = A_R = A/2$. Then,*

- 1) *If \mathcal{P}_α and \mathcal{P}_β are $\mathcal{U}[-1/2, 1/2]$ and $\phi_{1:G_\theta}$ is a uniform grid in $\sin \theta$ domain with a spacing of $2\lambda/A$, then (26) is satisfied.*
- 2) *If \mathcal{P}_p is $\mathcal{U}\{0, 1, \dots, P_{max} - 1\}$ and $\rho_{1:G_D}$ is a uniform grid of spacing $\lambda/(2P_{max}T_c)$, then (25) is satisfied.*

Proof: See Appendix E. ■

In Proposition 5, if $\phi_{1:G_\theta}$ covers the entire $[-\pi/2, \pi/2]$ interval, then $G_\theta = (A/\lambda) + 1$ where A/λ is the normalized array aperture. However, in practice, the radar focuses on a specific angular sector in each CPI. Similarly, denote $v_{max} = \lambda/4T_c$ as the maximum target velocity that can be detected by the given radar system. If $\rho_{1:G_D}$ covers $[-v_{max}, v_{max}]$ interval, then $G_D = P_{max} + 1$. Interestingly, the velocity resolution is then $\lambda/(2P_{max}T_c)$, same as the traditional radar transmitting P_{max} chirps. However, the proposed framework achieves this resolution by transmitting only $P < P_{max}$ chirps.

Finally, it is trivial to show that the non-uniform recovery condition (32) can be satisfied if \mathcal{P}_p is chosen as a discrete uniform distribution and either one of \mathcal{P}_α or \mathcal{P}_β is uniformly distributed. In this case, if \mathcal{P}_α is uniform, the receivers' locations $\beta_{1:N_R}$ can be chosen as a deterministic function of $\alpha_{1:N_T}$ (e.g., $\alpha_n = \beta_n$) and vice versa. Intuitively, both (25)-(26) and (32) impose that the grid points are placed at the zeros of the respective characteristic functions.

V. SIMULATION RESULTS

We compare the detection and estimation performance of our proposed methods with the classical-DFT and MUSIC techniques.

TABLE I: Simulation Parameters

Parameter	Value
Carrier Frequency f_c	24 GHz
Chirp Bandwidth $B = \gamma T_c$	250 MHz
Chirp Duration T_c	40 μ s
Sampling frequency f_s	5 MHz
Number of Chirps	$P = 10, P_{max} = 32$
Aperture Length	$A_T = A_R = 6\lambda$
Number of antenna elements in ULA	$N_T = 4, N_R = 8$
Number of antenna elements in SLA	$N_T = 2, N_R = 4$

Section V-A considers various range estimation methods while Section V-B focuses on the overall performance and time-complexity of various methods. The simulation parameters are listed in Table I. For SLA, $\alpha_n, \beta_m \sim \mathcal{U}[-1/2, 1/2]$ for all $1 \leq n \leq N_T$ and $1 \leq m \leq N_R$. For ULA, we consider the MIMO array setup of [12] wherein two transmitters are placed on either side of the array with λ spacing, and the receivers are placed between them with 0.5λ and 0.25λ spacings with one another and the transmitters, respectively. This arrangement results in 20 unique virtual array channels. Similarly, for the sparsely transmitted chirps, $\zeta_{1 \leq p \leq P}$ are chosen uniformly and independently from $\{0, 1, \dots, P_{max} - 1\}$ without replacement, while the classical FMCW setup transmits all P_{max} chirps. The target gains are generated as $a_k = \exp(j\psi_k)$ with $\psi_k \sim \mathcal{U}[0, 2\pi)$ (without any path loss) while the noise $w_{n,m,p}[t] \sim \mathcal{CN}(\mathbf{0}, \sigma^2 I)$, i.i.d. across all chirps and virtual array channels. Note that the SNR is $-10 \log_{10}(\sigma^2)$ [31].

A. DFT-focusing and Range-OMP

Consider three close range targets with ranges $R_1 = 48.8\text{m}$, $R_2 = 50.0\text{m}$ and $R_3 = 51.2\text{m}$ for the full measurements radar setup. For the parameters given in Table I, the range resolution for the DFT processing is 0.6m. In range-OMP, we choose a uniform grid $\omega_{1 \leq g \leq G_R}$ covering ranges 1.2m to 120m with resolution 0.12m. Both the binary and coherent integration process all 20×32 measurements $y_{n,m,p}$, but binary integration applies a 1/3-rd majority rule to filter valid target ranges. Contrarily, range-OMP considers only $y_{1,1,1}$ channel.

Fig. 2 shows the normalized range channels for DFT (with coherent and binary integration) and range-OMP. Fig. 2a & b indicate that only two targets are detected in coherent processing and Channel-A of binary processing. However, in the case of binary integration, the missed target is detected at Channel-B in Fig. 2c. On the contrary, the range-OMP in Fig. 2d recovers all three targets at a higher resolution using only $y_{1,1,1}$. Hence, range-OMP provides better estimates at lower complexity than DFT. Note that binary integration enhances performance only at low SNRs and exhibits the same performance as the coherent one at higher SNRs. Similarly, range-OMP followed by binary integration can be used to detect ranges from all $\{y_{n,m,p}\}$

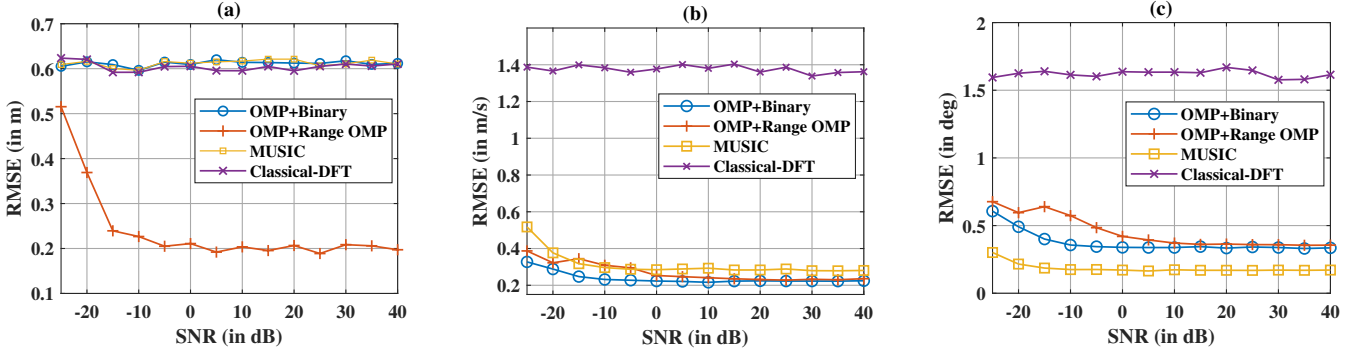


Fig. 3: RMSE in (a) range, (b) velocity, and (c) AOA estimation at different SNRs for the OMP+Binary, OMP+Range-OMP, classical-DFT and MUSIC methods.

TABLE II: Various parameter estimation methods

Method	Radar	Description
Classical-DFT	ULA with P_{max} chirps	DFT in range, Doppler and angular domains
MUSIC	ULA with P_{max} chirps	DFT in range and 2D-MUSIC with spatial smoothing [12] in Doppler-angle domain
OMP+Binary	SLA with sparse P chirps	DFT focusing with binary integration for range and 1D-OMP with (19) for velocity & AOA
OMP+Range-OMP	SLA with sparse P chirps	Range-OMP and 1D-OMP with (19) for velocity & AOA
2D-OMP	SLA with sparse P chirps	DFT-with-binary for range and 2D-OMP with (18) for velocity & AOA
BP	SLA with sparse P chirps	DFT-with-binary for range and 1D-BP with (19) for velocity & AOA
LASSO	SLA with sparse P chirps	DFT-with-binary for range and 1D-LASSO with (19) for velocity & AOA

measurements, resulting in enhanced detection at low SNRs but with increased computational costs. Throughout our experiments, we consider the range-OMP for $y_{1,1,1}$ only.

B. Range, velocity and AOA estimation

We consider $K = 5$ targets with uniformly drawn ranges $R_k \in [20 \text{ m}, 120 \text{ m}]$, velocities $v_k \in [-78 \text{ m/s}, 78 \text{ m/s}]$ and AOAs $\theta_k \in [-20^\circ, 20^\circ]$. We compare our proposed CS-based methods for SLA and sparse chirps with the conventional full-measurement radar systems in terms of detection probabilities, estimation errors, ROC, and run-time complexity. Table-II describes various methods considered for comparison. For classical-DFT, the range, velocity, and angular resolutions are 0.6m, 4.88 m/s, and 7° , respectively, for the parameters given in Table I. In range-OMP, a grid of resolution 0.12m is chosen as in Section V-V-A. Similarly, the velocity grid $\rho_{1 \leq g \leq G_D}$ is constructed using 200 uniform points in $[-78 \text{ m/s}, 78 \text{ m/s}]$ with resolution 0.78 m/s. The angular grid $\phi_{1 \leq g \leq G_\theta}$ is a uniform grid (in $\sin \theta$ domain) of 50 points in $[-30^\circ, 30^\circ]$ resulting in an approximate angular resolution of 2° . The CS-based AOA estimation method proposed in [31] (for pulsed-wave radars) assumes a known sparsity level and uses prior knowledge of the actual number of targets K in the CS algorithms. On the contrary, in 1D-OMP (19) and 2D-OMP (18) methods, we consider a sparsity level of $K_{max} = 20$ to terminate the algorithms, while BP and LASSO consider 100 iterations. A threshold detection is then used to obtain the target velocities and AOAs from the recovered signal.

Since different methods have different range, Doppler and angular resolutions, we investigate the target detection and parameter estimation performances separately. To this end, we define a detected target as ‘hit’ if the estimated range, velocity, and AOA from a given method are within the corresponding resolution from the true target parameters. Otherwise, it is a false alarm. We compare the hit rates of various methods to demonstrate target detection performance while

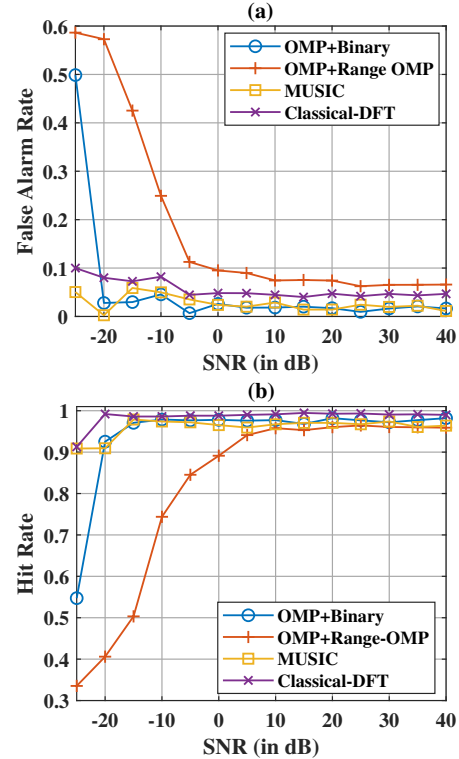


Fig. 4: (a) False-alarm, and (b) hit rates at different SNRs for OMP+Binary, OMP+Range-OMP, classical-DFT, and MUSIC.

different thresholds are set to maintain a constant false-alarm rate at all SNRs. For parameter estimation, we compute root-mean-squared estimation error (RMSE) for the targets classified as hits. Unless mentioned otherwise, the rates and RMSEs are averaged over 300 independent runs.

1) Comparison with classical-DFT & MUSIC: Fig. 4 compares the false-alarm and hit rates of various methods over -25dB to 40dB SNRs. The corresponding range, velocity, and angle RMSEs are shown in Fig. 3. Fig. 4 demonstrates that our proposed ‘OMP+Binary’ method achieves similar false-alarm and hit rates as the classical-DFT and MUSIC for all SNRs, but with only half the number of antenna elements and less than half transmitted chirps. In particular, OMP’s sparse radar setup considers 6 elements (2 transmitters and 4 receivers), while the classical-DFT and MUSIC consider a ULA of 12 elements (4 transmitters and 8 receivers). Similarly, the conventional setup transmits 32 chirps in a CPI, while in the sparse scenario, only 10 are transmitted randomly. Range-OMP provides similar performance only at high SNRs, but at lower computational costs

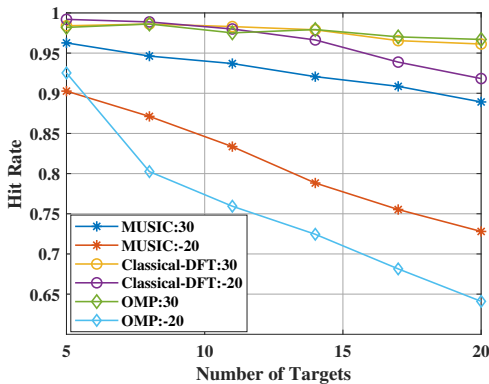


Fig. 5: Hit rate with varying number of targets K at SNR= 30dB, & -20dB, for OMP+Binary, classical-DFT and MUSIC.

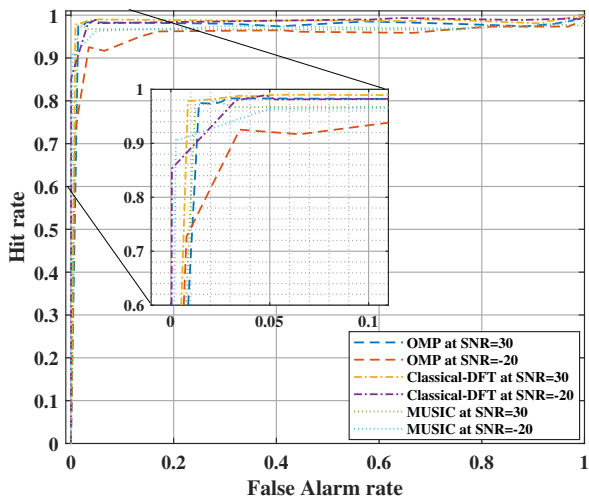


Fig. 6: ROC curves for OMP+Binary, classical-DFT, and MUSIC methods at 30dB and -20 dB SNRs.

than DFT-focusing as indicated in Table III.

In Fig. 3a, range-OMP, owing to its fine-resolution grid, exhibits significantly lower range estimation error than the DFT approach employed in other methods. Similarly, in Fig. 3b-c, the fine-resolution velocity and angle grids result in lower RMSEs than classical-DFT, but comparable to MUSIC. However, MUSIC, being a subspace-based approach, provides higher resolution with full measurements and higher computational costs.

2) Variation with number of targets: Fig. 5 shows the hit rate for different number of targets K at 30dB and -20 dB SNRs, for OMP+Binary, classical-DFT and MUSIC methods. The false-alarm rate is kept constant at 0.05. At high SNR, our proposed OMP method surpasses MUSIC with a hit rate greater than 0.95, like classical DFT. As K increases, MUSIC's hit rate decreases because of the fixed smoothing parameters and higher correlation among targets. On the other hand, OMP and classical-DFT maintain a near-constant hit rate. At very low SNR (-20 dB), both OMP and MUSIC's hit rate degrades rapidly with K , unlike classical-DFT. While at 30dB SNR, our proposed method surpasses MUSIC for all K , MUSIC exceeds at -20 dB. OMP's recovery depends heavily on the measurement matrices and hence, the velocity and angular grids. A coarser grid with small correlation among dictionary elements can enhance the hit rate at low SNRs, trading off resolution.

3) ROCs: Fig. 6 shows the ROCs for OMP+Binary, classical-DFT and MUSIC methods at 30dB and -20 dB SNRs. All methods exhibit near-ideal ROCs at both low and high SNRs. Unlike classical-DFT,

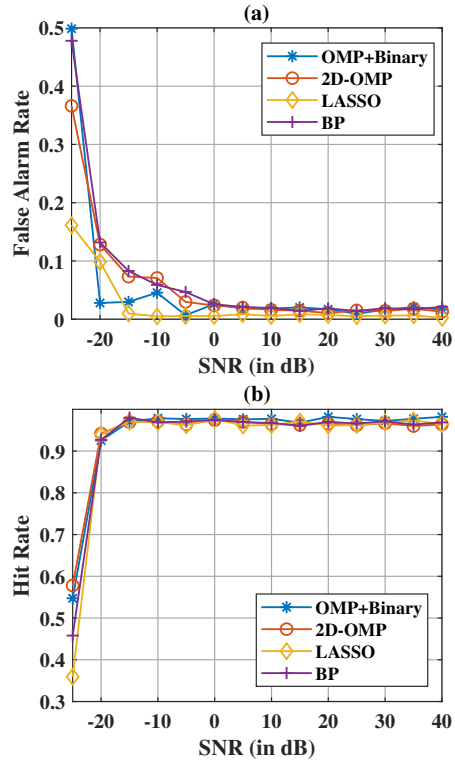


Fig. 7: (a) False alarm and (b) hit rates at different SNRs for OMP+Binary, 2D-OMP, BP, and LASSO methods.

TABLE III: Run-time for different methods (at 15dB SNR)

Method	Run time (in s)
Classical-DFT	0.2965
MUSIC	0.6592
OMP+Binary	0.2694
OMP+Range-OMP	0.1582
2D-OMP	0.1037
BP	1.9015
LASSO	0.1963

the detection performance of MUSIC and OMP degrades slightly at -20 dB SNR, with OMP's ROC being below MUSIC. However, as mentioned earlier, MUSIC processes measurements from a 4×8 ULA and all 32 transmitted chirps, while our method considers only a 2×4 SLA and 10 chirps in a CPI. Furthermore, from Table III, MUSIC has approximately 2.5 times longer run-time than OMP.

4) Comparison of different CS methods: Fig. 7 illustrates the false-alarm and hit rates of 1-D OMP, BP, and LASSO as well as 2D-OMP methods. Because of the same velocity and angular grids, the RMSEs of these methods are the same and, hence, omitted here. All algorithms exhibit similar false-alarm and hit rates for high SNRs (≥ 0 dB). On the other hand, at low SNRs (-20 dB to 0dB), LASSO achieves the same hit rate as other methods at the lowest false-alarm rate and hence, is more robust to noise. However, these methods differ in run-time complexity as elaborated in the following.

5) Time complexity: Table III provides the run-time (for one run) for various methods listed in Table II. As expected, MUSIC exhibits the longest run-time even though it provides high resolutions. The classical-DFT and OMP+Binary methods demonstrate similar time complexity, but OMP is more accurate, as indicated in Fig. 3. Range-OMP further reduces the run-time of our method because it considers only measurement $y_{1,1,1}$ for range detection, see Section V-A. Among different CS methods, 2D-OMP significantly outperforms the 1D OMP, BP, and LASSO algorithms. Overall, our CS-based methods,

with 2D-OMP being the most efficient, achieve similar hit rates but higher resolutions than classical methods, even with limited measurements. Our range-OMP further outperforms DFT-based range processing in terms of both resolution and computational costs.

VI. SUMMARY

We have developed CS-based range, velocity, and AOA estimation algorithms for MIMO-FMCW radar with random SLA and sparsely transmitted chirps. We proposed two different range estimation techniques: (a) DFT-focusing with binary integration, which enhances detection at low SNRs, and (b) range-OMP, which provides higher resolution and lower computational complexity. For joint Doppler-angle estimation, we considered both 1D-vectorized CS (OMP, BP, and LASSO) and 2D-OMP methods, wherein 2D-OMP directly estimates target parameters with lower complexity. Our numerical experiments show that these CS-based methods achieve the same performance as the classical-DFT and MUSIC approaches, but with fewer transmitter and receiver elements and less than half transmitted chirps. For joint Doppler-angle estimation, 2D-OMP provides higher resolutions than classical methods with superior efficiency, while range-OMP surpasses DFT-based processing in both resolution and computational efficiency. Our theoretical analysis further demonstrated that the required number of chirps and antenna elements scales linearly with the number of targets and logarithmically with the grid points, offering high resolutions with fewer measurements. Unlike uniform recovery, the non-uniform recovery guarantee provides flexibility in trading off between Doppler and angular measurements through a joint lower bound on chirps and antenna elements.

APPENDIX A PROOF OF LEMMA 1

Consider the (i_1, i_2) -th element of \mathbf{Q}_B as $[\mathbf{Q}_B]_{i_1, i_2}$. Recall from Section IV that any column of matrix \mathbf{B} is given by $\mathbf{b}(\rho_i) = [\exp(j\frac{4\pi T_c}{\lambda}\rho_i\zeta_1), \dots, \exp(j\frac{4\pi T_c}{\lambda}\rho_i\zeta_P)]^T$ such that

$$[\mathbf{Q}_B]_{i_1, i_2} = \mathbf{B}_{:, i_1}^H \mathbf{B}_{:, i_2} = \sum_{p=1}^P \exp\left(j\frac{4\pi T_c}{\lambda}(\rho_{i_2} - \rho_{i_1})\zeta_p\right).$$

If $\rho_{1:G_D}$ is a uniform grid, then $\rho_{i_2} - \rho_{i_1}$ is constant whenever $i_2 - i_1$ is constant, i.e., along every diagonal of \mathbf{Q}_B . Hence, \mathbf{Q}_B is a Toeplitz matrix. Also, using $i_1 = i_2$, we obtain all the main diagonal elements of \mathbf{Q}_B as P . Similarly, any column of matrix \mathbf{C} is given by $\mathbf{c}(\phi_i) = [\exp(j\frac{\pi A}{\lambda}\sin\phi_i(\alpha_1 + \beta_1)), \dots, \exp(j\frac{\pi A}{\lambda}\sin\phi_i(\alpha_{N_T} + \beta_{N_R}))]^T$. Hence, under the uniform grid assumption, \mathbf{Q}_C can also be proved to be a Toeplitz matrix with all main diagonal elements as $N_T N_R$ following similar arguments.

APPENDIX B PROOF OF THEOREM 1

Appendix B-A provides some preliminary results, including suitable bounds on Γ_B and Γ_C . The bound on coherence μ is then derived in Appendix B-B.

A. Preliminaries

Lemma 2. Consider a radar transmitting P chirps randomly over a total CPI comprising of P_{max} chirps duration. Let the chirps' indices $\zeta_{1:P} \in \{0, 1, \dots, P_{max} - 1\}$ be distributed as \mathcal{P}_p , which is symmetrical about $(P_{max} - 1)/2$. If \mathcal{P}_p and uniform grid $\rho_{1:G_D}$ satisfy (25), then

$$\mathbb{P}\left(\frac{1}{P}|\mathbf{B}_{:, i}^H \mathbf{B}_{:, i}| > \vartheta\right) = e^{-\vartheta^2 P},$$

where $0 < \vartheta < 1$ and $i = 2, 3, \dots, G_D$.

Proof: Define $\zeta'_p = \zeta_p - \frac{P_{max}-1}{2}$. Substituting this in (22), we obtain $\Gamma_B(u) = \exp(ju\frac{P_{max}-1}{2})\Gamma'_B(u)$ where $\Gamma'_B(u) = \frac{1}{P}\sum_{p=1}^P \exp(ju\zeta'_p)$. Now, since $\zeta_p \sim \mathcal{P}_p(\cdot)$, the random variable ζ'_p has an even distribution because $\mathcal{P}_p(\cdot)$ is symmetric about $(P_{max} - 1)/2$. Consequently, $\Gamma'_B(u)$ is asymptotically jointly Gaussian distributed [56, Sec. II] as

$$\begin{bmatrix} \text{Re } \Gamma'_B \\ \text{Im } \Gamma'_B \end{bmatrix} \sim \mathcal{N}\left(\begin{bmatrix} \text{Re } \Psi_{p'} \\ \text{Im } \Psi_{p'} \end{bmatrix}, \begin{bmatrix} \sigma_1^2 & 0 \\ 0 & \sigma_2^2 \end{bmatrix}\right),$$

where $\sigma_1^2(u) = \frac{1}{2P}(1 + \Psi_{p'}(2u)) - \frac{1}{P}\Psi_{p'}(u)^2$ and $\sigma_2^2(u) = \frac{1}{2P}(1 - \Psi_{p'}(2u))$ with $\Psi_{p'}(\cdot)$ denoting the characteristic function given by $\Psi_{p'}(u) = \mathbb{E}_{\zeta \sim \mathcal{P}_p}[\exp(ju(\zeta - \frac{P_{max}-1}{2}))] = \exp(-ju\frac{P_{max}-1}{2})\Psi_p(u)$. Further using (25), we obtain $\Psi_{p'}(u_{1,i}^D) = \Psi_{p'}(2u_{1,i}^D) = 0$ for $i = 2, 3, \dots, G_D$. Hence, for $u = u_{1,i}^D$, Γ'_B is Gaussian distributed as

$$\begin{bmatrix} \text{Re } \Gamma'_B \\ \text{Im } \Gamma'_B \end{bmatrix} \sim \mathcal{N}\left(\begin{bmatrix} 0 \\ 0 \end{bmatrix}, \begin{bmatrix} 1/2P & 0 \\ 0 & 1/2P \end{bmatrix}\right),$$

which implies $|\Gamma'_B|$ is Rayleigh distributed with $\sigma^2 = 1/2P$.

Now, $|\Gamma_B(u)| = |\exp(ju\frac{P_{max}-1}{2})| \times |\Gamma'_B(u)| = |\Gamma'_B(u)|$. Therefore, for $u = u_{1,i}^D$, $|\Gamma_B|$ is also Rayleigh distributed with $\sigma^2 = 1/2P$. Finally, using (22) and $\|\mathbf{B}_{:, i}\|_2 = \sqrt{P}$, we have

$$\mathbb{P}\left(\frac{1}{P}|\mathbf{B}_{:, i}^H \mathbf{B}_{:, i}| > \vartheta\right) = \mathbb{P}(|\Gamma_B(u_{1,i}^D)| > \vartheta) = e^{-\vartheta^2 P},$$

where the last equality follows from the complementary cdf of a Rayleigh distribution. ■

Lemma 3. Consider a MIMO radar with random SLA as described in Section II with $\alpha_{1:N_T}$ and $\beta_{1:N_R}$ drawn i.i.d. from even distributions \mathcal{P}_α and \mathcal{P}_β , respectively. If \mathcal{P}_α , \mathcal{P}_β and the uniform grid $\phi_{1:G_\theta}$ satisfy (26), then for $0 < \vartheta < 1$ and $i = 2, 3, \dots, G_\theta$,

1) If $\alpha_{1:N_T}$ and $\beta_{1:N_R}$ are independent, we have:

$$\mathbb{P}\left(\frac{1}{N_T N_R}|\mathbf{C}_{:, i}^H \mathbf{C}_{:, i}| > \vartheta\right) < 2\vartheta\sqrt{N_T N_R}\mathcal{K}_1(2\vartheta\sqrt{N_T N_R}),$$

where $\mathcal{K}_1(\cdot)$ is the modified Bessel function of second kind.

2) If $N_T = N_R$ and $\alpha_n = \beta_n$ for all $1 \leq n \leq N_T$,

$$\mathbb{P}\left(\frac{1}{N_T^2}|\mathbf{C}_{:, i}^H \mathbf{C}_{:, i}| > \vartheta\right) = e^{-N_T \vartheta}.$$

Proof: The lemma is obtained trivially by generalizing the results of [31, Theorem 1] to the MIMO-FMCW radar array. ■

B. Proof of the theorem

As a consequence of Lemma 1 and substituting $\|\mathbf{B}_{:, i}\|_2 = \sqrt{P}$ and $\|\mathbf{C}_{:, j}\| = \sqrt{N_T N_R}$ in (24), we obtain

$$\mu \leq \max\{\max_{i>1} \frac{1}{P}|\mathbf{B}_{:, i}^H \mathbf{B}_{:, i}|, \max_{j>1} \frac{1}{N_T N_R}|\mathbf{C}_{:, j}^H \mathbf{C}_{:, j}|\}.$$

Hence, we can bound $\mathbb{P}(\mu \leq \vartheta)$ as

$$\begin{aligned} \mathbb{P}(\mu \leq \vartheta) &\geq \mathbb{P}\left(\max\{\max_{i>1} \frac{1}{P}|\mathbf{B}_{:, i}^H \mathbf{B}_{:, i}|, \max_{j>1} \frac{1}{N_T N_R}|\mathbf{C}_{:, j}^H \mathbf{C}_{:, j}|\} \leq \vartheta\right) \\ &= \mathbb{P}\left(\max_{i>1} \frac{1}{P}|\mathbf{B}_{:, i}^H \mathbf{B}_{:, i}| \leq \vartheta\right) \mathbb{P}\left(\max_{j>1} \frac{1}{N_T N_R}|\mathbf{C}_{:, j}^H \mathbf{C}_{:, j}| \leq \vartheta\right) \\ &= \mathbb{P}\left(\frac{1}{P}|\mathbf{B}_{:, i}^H \mathbf{B}_{:, i}| \leq \vartheta \forall i > 1\right) \mathbb{P}\left(\frac{1}{N_T N_R}|\mathbf{C}_{:, j}^H \mathbf{C}_{:, j}| \leq \vartheta \forall j > 1\right) \\ &= \mathbb{P}\left(\frac{1}{P}|\mathbf{B}_{:, i}^H \mathbf{B}_{:, i}| \leq \vartheta\right)^{G_D-1} \mathbb{P}\left(\frac{1}{N_T N_R}|\mathbf{C}_{:, j}^H \mathbf{C}_{:, j}| \leq \vartheta\right)^{G_\theta-1}, \end{aligned}$$

because $\mathbf{B}_{:, i}^H \mathbf{B}_{:, i}$ and $\mathbf{C}_{:, j}^H \mathbf{C}_{:, j}$ are mutually independent and identically distributed for all $i = 2, 3, \dots, G_D$ and $j = 2, 3, \dots, G_\theta$, respectively. Finally, using $\mathbb{P}(\mu > \vartheta) = 1 - \mathbb{P}(\mu \leq \vartheta)$ and Lemmas 2-3, we obtain (27) and (28), respectively, when $\alpha_{1:N_T}$ and $\beta_{1:N_R}$ are independent and $\alpha_n = \beta_n \forall n$.

APPENDIX C
PROOF OF THEOREM 2

According to [52, Theorem 2.7], any K -sparse signal can be recovered if the measurement matrix \mathbf{D} has RIP constant $\delta_{2K} < 2/(3 + \sqrt{7/4}) \doteq \Lambda$. Hence, we need to bound δ_{2K} with a probability higher than $1 - \epsilon$, or equivalently, $\mathbb{P}(\delta_{2K} > \Lambda) < \epsilon$ where $0 < \epsilon < 1$. However, RIP constant δ_{2K} and coherence μ of a matrix satisfy $\delta_{2K} \leq (2K - 1)\mu$ [52]. Hence, $\mathbb{P}(\delta_{2K} > \Lambda) \leq \mathbb{P}(\mu > \Lambda/(2K - 1))$.

We first consider the case when $\alpha_{1:N_T}$ and $\beta_{1:N_R}$ are independent. Using (27), we obtain

$$\mathbb{P}(\delta_{2K} > \Lambda) < 1 - (1 - e^{-\vartheta_0^2 P})^{G_D - 1} \times (1 - 2\vartheta_0 \sqrt{N_T N_R} \mathcal{K}_1(2\vartheta_0 \sqrt{N_T N_R}))^{G_\theta - 1}, \quad (35)$$

where $\vartheta_0 = \Lambda/(2K - 1)$. Now, we need to find the number of chirps P and antenna elements $N_T N_R$ such that the R.H.S. of (35) is less or equal to ϵ . To this end, we approximate the Bessel function as $\mathcal{K}_1(q) \approx \sqrt{\frac{\pi}{2q}} \exp(-q)$ [57] such that

$$\begin{aligned} 1 - (1 - e^{-\vartheta_0^2 P})^{G_D - 1} (1 - 2\vartheta_0 \sqrt{N_T N_R} \mathcal{K}_1(2\vartheta_0 \sqrt{N_T N_R}))^{G_\theta - 1} \\ \approx 1 - (1 - e^{-\vartheta_0^2 P})^{G_D - 1} (1 - (\pi^2 \vartheta_0^2 N_T N_R)^{1/4} e^{-2\vartheta_0 \sqrt{N_T N_R}})^{G_\theta - 1} \\ \approx 1 - (1 - G_D e^{-\vartheta_0^2 P}) (1 - G_\theta (\pi^2 \vartheta_0^2 N_T N_R)^{1/4} e^{-2\vartheta_0 \sqrt{N_T N_R}}), \end{aligned}$$

where the last approximation is obtained using $(1 - x)^n \approx 1 - nx$ and $G_\theta, G_D \gg 1$. Hence, R.H.S. of (35) $\leq \epsilon$ implies

$$(1 - G_D e^{-\vartheta_0^2 P}) (1 - G_\theta (\pi^2 \vartheta_0^2 N_T N_R)^{1/4} e^{-2\vartheta_0 \sqrt{N_T N_R}}) \geq 1 - \epsilon.$$

Expanding L.H.S. with $G_D G_\theta (\pi^2 \vartheta_0^2 N_T N_R)^{1/4} \exp(-\vartheta_0^2 P) \times \exp(-2\vartheta_0 \sqrt{N_T N_R}) \approx 0$, we obtain

$$G_D \exp(-\vartheta_0^2 P) + G_\theta (\pi^2 \vartheta_0^2 N_T N_R)^{1/4} \exp(-2\vartheta_0 \sqrt{N_T N_R}) \leq \epsilon,$$

which is satisfied if $G_D \exp(-\vartheta_0^2 P) \leq \epsilon_1$ and $G_\theta (\pi^2 \vartheta_0^2 N_T N_R)^{1/4} \exp(-2\vartheta_0 \sqrt{N_T N_R}) \leq \epsilon_2$ with $\epsilon_1 + \epsilon_2 = \epsilon$.

Now, rearranging $G_D \exp(-\vartheta_0^2 P) \leq \epsilon_1$ and substituting $\vartheta_0 = \Lambda/(2K - 1)$, we obtain $P \geq \frac{4}{\Lambda^2} (K - \frac{1}{2})^2 \log\left(\frac{G_D}{\epsilon_1}\right)$, which is (29). On the other hand, rearranging $G_\theta (\pi^2 \vartheta_0^2 N_T N_R)^{1/4} \exp(-2\vartheta_0 \sqrt{N_T N_R}) \leq \epsilon_2$, we obtain

$$-4\vartheta_0 \sqrt{N_T N_R} \exp(-4\vartheta_0 \sqrt{N_T N_R}) \geq -\left(\frac{2\epsilon_2}{G_\theta \sqrt{\pi}}\right)^2,$$

which can be solved using Lambert W function [58] as in the proof of [31, Theorem 2] to obtain (30). The constants κ_1 and κ_2 in (29)-(30) are obtained by substituting $\Lambda = 2/(3 + \sqrt{7/4})$.

For the case when $\alpha_n = \beta_n$, we have $\mathbb{P}(\delta_{2K} > \Lambda) < 1 - (1 - e^{-\vartheta_0^2 P})^{G_D - 1} (1 - e^{-N_T \vartheta_0})^{G_\theta - 1}$ using (28) with $\vartheta_0 = \Lambda/(2K - 1)$. Again, using $(1 - x)^n \approx 1 - nx$ and $G_D, G_\theta \gg 1$ and following similar steps as in the independent $\alpha_{1:N_T}$ and $\beta_{1:N_R}$ case, we obtain $G_D e^{-\vartheta_0^2 P} + G_\theta e^{-N_T \vartheta_0} \leq \epsilon$, which is satisfied if $G_D e^{-\vartheta_0^2 P} \leq \epsilon_1$ and $G_\theta e^{-N_T \vartheta_0} \leq \epsilon_2$ with $\epsilon_1 + \epsilon_2 = \epsilon$. Rearranging these inequalities, we obtain (29) and (31), respectively. Finally, the claim of the theorem then follows from [52, Theorem 2.7] considering the exact K -sparse signal case.

APPENDIX D
PROOF OF THEOREM 3

If part: Using $\mathbf{D}_{N_T N_R(i-1)+j,:} = \mathbf{B}_{i,:} \otimes \mathbf{C}_{j,:}$, we obtain $\mathbb{E}[\mathbf{D}_{i,:}^H \mathbf{D}_{l,:}] = \mathbb{E}[\mathbf{B}_{i,:}^H \mathbf{B}_{l,:}] \otimes \mathbb{E}[\mathbf{C}_{j,:}^H \mathbf{C}_{j,:}]$ for some $1 \leq i \leq P$ and $1 \leq j \leq N_T N_R$ because $\zeta_{1:P}$ is independent of $\alpha_{1:N_T}$ and $\beta_{1:N_R}$. We first consider $[\mathbf{B}_{i,:}^H \mathbf{B}_{i,:}]$. Here, $\zeta_{1:P}$ are identically distributed such that $\mathbb{E}[\mathbf{B}_{i,:}^H \mathbf{B}_{i,:}]$ does not depend on row index i and $\mathbb{E}[\mathbf{B}_{i,:}^H \mathbf{B}_{i,:}] = \frac{1}{P} \sum_{i=1}^P \mathbb{E}[\mathbf{B}_{i,:}^H \mathbf{B}_{i,:}]$. But, by simple comparison of matrix elements, we can show that $\sum_{i=1}^P \mathbb{E}[\mathbf{B}_{i,:}^H \mathbf{B}_{i,:}] = \mathbf{Q}_B$. Hence,

$\mathbb{E}[\mathbf{B}_{i,:}^H \mathbf{B}_{i,:}] = \tilde{\mathbf{Q}}_B$ where $\tilde{\mathbf{Q}}_B = (1/P) \mathbb{E}[\mathbf{Q}_B]$. As a consequence of Lemma 1, we only consider the first row of $\tilde{\mathbf{Q}}_B$. Note that $(1, i)$ -th element of \mathbf{Q}_B is $\mathbf{B}_{i,:}^H \mathbf{B}_{i,:} = P \Gamma_B(u_{1,i}^D)$ using (22). Hence, for $1 \leq i \leq G_D$,

$$\begin{aligned} [\tilde{\mathbf{Q}}_B]_{1,i} &= \mathbb{E}[\Gamma_B(u_{1,i}^D)] = \frac{1}{P} \sum_{p=1}^P \mathbb{E}[\exp(ju_{1,i}^D \zeta_p)] \\ &= \frac{1}{P} \sum_{p=1}^P \mathbb{E}[\exp(ju_{1,i}^D \zeta)] = \Psi_p(u_{1,i}^D) \end{aligned}$$

where the second-last equality follows because ζ_p are i.i.d. for all $1 \leq p \leq P$. Finally, if $\Psi_p(u_{1,i}^D) = 0$ for $i = 2, 3, \dots, G_D$ according to (32), then $\mathbb{E}[\mathbf{B}_{i,:}^H \mathbf{B}_{i,:}] = \mathbf{Q}_B = \mathbf{I}_{G_D}$. Note that $[\tilde{\mathbf{Q}}_B]_{1,1} = 1$ because all main diagonal elements of \mathbf{Q}_B is P from Lemma 1. Further, following similar steps as in proof of [31, Theorem 3], we can trivially show that $\mathbb{E}[\mathbf{C}_{j,:}^H \mathbf{C}_{j,:}] = \mathbf{I}_{G_\theta}$ if $\Psi_\xi(u_{1,j}^D) = 0$ for $j = 2, 3, \dots, G_\theta$ as in (32). Finally, $\mathbb{E}[\mathbf{D}_{l,:}^H \mathbf{D}_{l,:}] = \mathbb{E}[\mathbf{B}_{i,:}^H \mathbf{B}_{i,:}] \otimes \mathbb{E}[\mathbf{C}_{j,:}^H \mathbf{C}_{j,:}] = \mathbf{I}_{G_D} \otimes \mathbf{I}_{G_\theta} = \mathbf{I}_{G_D G_\theta}$, i.e., if (32) holds, matrix \mathbf{D} satisfies isotropy property.

Only if part: If $\Psi_p(u_{1,i}^D) \neq 0$ for some $i = 2, 3, \dots, G_D$, then $[\tilde{\mathbf{Q}}_B]_{1,i} \neq 0$. Hence, $\mathbb{E}[\mathbf{B}_{i,:}^H \mathbf{B}_{i,:}] \neq \mathbf{I}$ which implies $\mathbb{E}[\mathbf{D}_{l,:}^H \mathbf{D}_{l,:}] \neq \mathbf{I}$, i.e., matrix \mathbf{D} does not satisfy isotropy property. Similarly, matrix \mathbf{D} also does not satisfy isotropy property if $\Psi_\xi(u_{1,j}^D) \neq 0$ for some $j = 2, 3, \dots, G_\theta$. Therefore, (32) is a necessary condition.

APPENDIX E

PROOF OF PROPOSITION 5

Note that $\alpha_{1:N_T}, \beta_{1:N_R} \in [-1/2, 1/2]$ when $A_T = A_R = A/2$ and the characteristic function of uniform distributions \mathcal{P}_α and \mathcal{P}_β are

$$\Psi_\alpha(u) = \Psi_\beta(u) = \frac{\sin(u/2)}{u/2}.$$

From (26), we need $\Psi_\alpha(u_{i,j}^\theta) = \Psi_\alpha(2u_{i,j}^\theta) = 0$ and $\Psi_\beta(u_{i,j}^\theta) = \Psi_\beta(2u_{i,j}^\theta) = 0$ for $i \neq j$ which can be satisfied if $u_{i,j}^\theta/2 = k\pi$ for some integer k . But, by definition, $\frac{u_{i,j}^\theta}{2} = \pi \frac{A}{2\lambda} (\sin \phi_j - \sin \phi_i)$. Hence, condition (26) is satisfied if $\phi_{1:G_\theta}$ is a uniformly spaced grid of spacing $2\lambda/A$ in the $\sin \theta$ domain.

For discrete uniform distribution \mathcal{P}_p , we have

$$\Psi_p(u) = \frac{1 - e^{jP_{max}u}}{P_{max}(1 - e^u)}.$$

We need $\Psi_p(u_{i,l}^D) = \Psi_p(2u_{i,l}^D) = 0$ for $i \neq l$ which is satisfied if $P_{max}u_{i,l}^D = 2k\pi$ for some integer k . But, $P_{max}u_{i,l}^D = 2\pi \cdot \frac{2P_{max}T_c}{\lambda} (\rho_l - \rho_i)$. Hence, (25) is satisfied when $\rho_{1:G_D}$ is a uniform grid of spacing $\lambda/(2P_{max}T_c)$.

REFERENCES

- [1] H. Singh and A. Chattopadhyay, "Multi-target range and angle detection for mimo-fmcw radar with limited antennas," in *2023 31st European Signal Processing Conference (EUSIPCO)*. IEEE, 2023, pp. 725–729.
- [2] S. Sun, A. P. Petropulu, and H. V. Poor, "MIMO radar for advanced driver-assistance systems and autonomous driving: Advantages and challenges," *IEEE Signal Processing Magazine*, vol. 37, no. 4, pp. 98–117, 2020.
- [3] S. M. Patole, M. Torlak, D. Wang, and M. Ali, "Automotive radars: A review of signal processing techniques," *IEEE Signal Processing Magazine*, vol. 34, no. 2, pp. 22–35, 2017.
- [4] A. Meta, P. Hoogeboom, and L. P. Ligthart, "Signal processing for FMCW SAR," *IEEE Transactions on Geoscience and Remote Sensing*, vol. 45, no. 11, pp. 3519–3532, 2007.
- [5] C. Gu, W. Chang, X. Li, G. Jia, and X. Luan, "A new distortion correction method for FMCW SAR real-time imaging," *IEEE Geoscience and Remote Sensing Letters*, vol. 14, no. 3, pp. 429–433, 2017.
- [6] S. Saponara and B. Neri, "Radar sensor signal acquisition and multi-dimensional FFT processing for surveillance applications in transport systems," *IEEE Transactions on Instrumentation and Measurement*, vol. 66, no. 4, pp. 604–615, 2017.

- [7] B.-s. Kim, Y. Jin, S. Kim, and J. Lee, "A low-complexity FMCW surveillance radar algorithm using two random beat signals," *Sensors*, vol. 19, no. 3, p. 608, 2019.
- [8] Z. Xu, C. Shi, T. Zhang, S. Li, Y. Yuan, C.-T. M. Wu, Y. Chen, and A. Petropulu, "Simultaneous monitoring of multiple people's vital sign leveraging a single phased-MIMO radar," *IEEE Journal of Electromagnetics, RF and Microwaves in Medicine and Biology*, vol. 6, no. 3, pp. 311–320, 2022.
- [9] R. Feger, C. Wagner, S. Schuster, S. Scheibhofer, H. Jager, and A. Stelzer, "A 77-GHz FMCW MIMO radar based on an SiGe single-chip transceiver," *IEEE Transactions on Microwave theory and Techniques*, vol. 57, no. 5, pp. 1020–1035, 2009.
- [10] M. A. Richards, *Fundamentals of radar signal processing*. McGraw-Hill Education, 2014.
- [11] G. O. Manokhin, Z. T. Erdyneev, A. A. Geltser, and E. A. Monastyr, "MUSIC-based algorithm for range-azimuth FMCW radar data processing without estimating number of targets," in *Mediterranean Microwave Symposium (MMS)*. IEEE, 2015, pp. 1–4.
- [12] F. Belfiori, W. van Rossum, and P. Hooeboom, "2D-MUSIC technique applied to a coherent FMCW MIMO radar," in *IET International Conference on Radar Systems (Radar 2012)*, 2012, pp. 1–6.
- [13] A. N. Lemma, A.-J. Van Der Veen, and E. F. Deprettere, "Analysis of joint angle-frequency estimation using ESPRIT," *IEEE Transactions on Signal Processing*, vol. 51, no. 5, pp. 1264–1283, 2003.
- [14] S. Kim, D. Oh, and J. Lee, "Joint DFT-ESPRIT estimation for TOA and DOA in vehicle FMCW radars," *IEEE Antennas and Wireless Propagation Letters*, vol. 14, pp. 1710–1713, 2015.
- [15] B. Friedlander and A. Zeira, "Eigenstructure-based algorithms for direction finding with time-varying arrays," *IEEE transactions on aerospace and electronic systems*, vol. 32, no. 2, pp. 689–701, 1996.
- [16] M. Elad, *Sparse and redundant representations: from theory to applications in signal and image processing*. Springer, 2010, vol. 2, no. 1.
- [17] R. Baraniuk and P. Steeghs, "Compressive radar imaging," in *2007 IEEE radar conference*. IEEE, 2007, pp. 128–133.
- [18] M. Herman and T. Strohmer, "Compressed sensing radar," in *2008 IEEE Radar Conference*. IEEE, 2008, pp. 1–6.
- [19] M. A. Herman and T. Strohmer, "High-resolution radar via compressed sensing," *IEEE transactions on signal processing*, vol. 57, no. 6, pp. 2275–2284, 2009.
- [20] C.-Y. Chen and P. Vaidyanathan, "Compressed sensing in mimo radar," in *2008 42nd Asilomar Conference on Signals, Systems and Computers*. IEEE, 2008, pp. 41–44.
- [21] L. C. Potter, E. Ertin, J. T. Parker, and M. Cetin, "Sparsity and compressed sensing in radar imaging," *Proceedings of the IEEE*, vol. 98, no. 6, pp. 1006–1020, 2010.
- [22] Y.-S. Yoon and M. G. Amin, "Compressed sensing technique for high-resolution radar imaging," in *Signal Processing, Sensor Fusion, and Target Recognition XVII*, vol. 6968. SPIE, 2008, pp. 506–515.
- [23] L. Anitori, A. Maleki, M. Otten, R. G. Baraniuk, and P. Hooeboom, "Design and analysis of compressed sensing radar detectors," *IEEE Transactions on Signal Processing*, vol. 61, no. 4, pp. 813–827, 2012.
- [24] I. Bilik, "Spatial compressive sensing for direction-of-arrival estimation of multiple sources using dynamic sensor arrays," *IEEE Transactions on Aerospace and Electronic Systems*, vol. 47, no. 3, pp. 1754–1769, 2011.
- [25] E. Tohidi, A. Hariri, H. Behroozi, M. M. Nayebi, G. Leus, and A. P. Petropulu, "Compressed-domain detection and estimation for colocated mimo radar," *IEEE Transactions on Aerospace and Electronic Systems*, vol. 56, no. 6, pp. 4504–4518, 2020.
- [26] O. Bar-Ilan and Y. C. Eldar, "Sub-Nyquist radar via Doppler focusing," *IEEE Transactions on Signal Processing*, vol. 62, no. 7, pp. 1796–1811, 2014.
- [27] D. Cohen, D. Cohen, Y. C. Eldar, and A. M. Haimovich, "SUMMeR: Sub-nyquist MIMO radar," *IEEE Transactions on Signal Processing*, vol. 66, no. 16, pp. 4315–4330, 2018.
- [28] K. V. Mishra, Y. C. Eldar, A. Maio, and A. Haimovich, "Sub-Nyquist radar: Principles and prototypes," in *Compressed sensing in radar signal processing*. Cambridge University Press, 2019, pp. 1–48.
- [29] S. Sun and A. P. Petropulu, "A sparse linear array approach in automotive radars using matrix completion," in *IEEE International Conference on Acoustics, Speech and Signal Processing (ICASSP)*. IEEE, 2020, pp. 8614–8618.
- [30] K. Diamantaras, Z. Xu, and A. Petropulu, "Sparse antenna array design for MIMO radar using softmax selection," *arXiv preprint arXiv:2102.05092*, 2021.
- [31] M. Rossi, A. M. Haimovich, and Y. C. Eldar, "Spatial compressive sensing for MIMO radar," *IEEE Transactions on Signal Processing*, vol. 62, no. 2, pp. 419–430, 2013.
- [32] Y. Yu, A. P. Petropulu, and H. V. Poor, "MIMO radar using compressive sampling," *IEEE Journal of Selected Topics in Signal Processing*, vol. 4, no. 1, pp. 146–163, 2010.
- [33] Y. Liu, Y. Zhang, J. Tang, N. Zhang, and W. Zhu, "Three dimensional compressive sensing in mimo radar," in *2015 49th Asilomar Conference on Signals, Systems and Computers*. IEEE, 2015, pp. 599–603.
- [34] A. Correias-Serrano and M. A. Gonzalez-Huici, "Sparse reconstruction of chirplets for automotive FMCW radar interference mitigation," in *2019 IEEE MTT-S International Conference on Microwaves for Intelligent Mobility (ICMIM)*, 2019, pp. 1–4.
- [35] D. Cohen, K. V. Mishra, and Y. C. Eldar, "Spectrum sharing radar: Coexistence via Xampling," *IEEE Transactions on Aerospace and Electronic Systems*, vol. 54, no. 3, pp. 1279–1296, 2017.
- [36] D. Ma, N. Shlezinger, T. Huang, Y. Liu, and Y. C. Eldar, "FRaC: FMCW-based joint radar-communications system via index modulation," *IEEE Journal of Selected Topics in Signal Processing*, vol. 15, no. 6, pp. 1348–1364, 2021.
- [37] Z. Cao, J. Li, C. Song, Z. Xu, and X. Wang, "Compressed sensing-based multitarget cfar detection algorithm for fmcw radar," *IEEE Transactions on Geoscience and Remote Sensing*, vol. 59, no. 11, pp. 9160–9172, 2021.
- [38] J. H. Ender, "On compressive sensing applied to radar," *Signal Processing*, vol. 90, no. 5, pp. 1402–1414, 2010.
- [39] J. De Wit, W. Van Rossum, and A. De Jong, *Orthogonal waveforms for FMCW MIMO radar*. IEEE, 2011.
- [40] G. Babur, O. A. Krasnov, A. Yarovoy, and P. Aubry, "Nearly orthogonal waveforms for MIMO FMCW radar," *IEEE Transactions on Aerospace and Electronic Systems*, vol. 49, no. 3, pp. 1426–1437, 2013.
- [41] L. Xu, S. Sun, K. V. Mishra, and Y. D. Zhang, "Automotive FMCW radar with difference co-chirps," *IEEE Transactions on Aerospace and Electronic Systems*, 2023.
- [42] V. Winkler, "Range doppler detection for automotive fmcw radars," in *2007 European Radar Conference*. IEEE, 2007, pp. 166–169.
- [43] Y. C. Eldar and G. Kutyniok, *Compressed sensing: theory and applications*. Cambridge university press, 2012.
- [44] Y. C. Pati, R. Rezaifar, and P. S. Krishnaprasad, "Orthogonal matching pursuit: Recursive function approximation with applications to wavelet decomposition," in *Proceedings of 27th Asilomar conference on Signals, Systems and Computers*. IEEE, 1993, pp. 40–44.
- [45] S. Chen, S. A. Billings, and W. Luo, "Orthogonal least squares methods and their application to non-linear system identification," *International Journal of Control*, vol. 50, no. 5, pp. 1873–1896, 1989.
- [46] D. Needell and J. A. Tropp, "CoSaMP: Iterative signal recovery from incomplete and inaccurate samples," *Applied and computational harmonic analysis*, vol. 26, no. 3, pp. 301–321, 2009.
- [47] E. J. Candès and M. B. Wakin, "An introduction to compressive sampling," *IEEE Signal Processing magazine*, vol. 25, no. 2, pp. 21–30, 2008.
- [48] R. Tibshirani, "Regression shrinkage and selection via the lasso," *Journal of the Royal Statistical Society Series B: Statistical Methodology*, vol. 58, no. 1, pp. 267–288, 1996.
- [49] Y. Fang, J. Wu, and B. Huang, "2d sparse signal recovery via 2d orthogonal matching pursuit," *Science China Information Sciences*, vol. 55, pp. 889–897, 2012.
- [50] Y. Liu, M. Wu, and S. Wu, "Fast OMP algorithm for 2D angle estimation in MIMO radar," *Electronics letters*, vol. 46, no. 6, pp. 444–445, 2010.
- [51] S. Foucart and H. Rauhut, *An invitation to compressive sensing*. Springer, 2013.
- [52] H. Rauhut, "Compressive sensing and structured random matrices," *Theoretical foundations and numerical methods for sparse recovery*, vol. 9, no. 1, p. 92, 2010.
- [53] M. Hügel, H. Rauhut, and T. Strohmer, "Remote sensing via 11-minimization," *Foundations of Computational Mathematics*, vol. 14, no. 1, pp. 115–150, 2014.
- [54] E. J. Candès and Y. Plan, "A probabilistic and RIPless theory of compressed sensing," *IEEE Transactions on Information Theory*, vol. 57, no. 11, pp. 7235–7254, 2011.
- [55] D. H. Johnson and D. E. Dudgeon, *Array Signal Processing: Concepts and Techniques*. Prentice-Hall, 1993.
- [56] Y. Lo, "A mathematical theory of antenna arrays with randomly spaced elements," *IEEE Transactions on Antennas and Propagation*, vol. 12, no. 3, pp. 257–268, 1964.
- [57] G. N. Watson, *A treatise on the theory of Bessel functions*. The University Press, 1922, vol. 2.
- [58] R. M. Corless, G. H. Gonnet, D. E. Hare, D. J. Jeffrey, and D. E. Knuth, "On the Lambert W function," *Advances in Computational mathematics*, vol. 5, pp. 329–359, 1996.